The Astrophysical Journal Letters, 992:L30 (21pp), 2025 October 20 https://doi.org/10.3847/2041-8213/ae0ccd
© 2025. The Author(s). Published by the American Astronomical Society.
OPEN ACCESS

Protostars at Subsolar Metallicity: First Detection of Large Solid-state Complex Organic Molecules in the Large Magellanic Cloud

Marta Sewiło[1,2,3], Will R. M. Rocha[4,5], Martijn van Gelder[5], Maria Gabriela Navarro[6], Steven B. Charnley[7], Miwha Jin[7,8], Joana M. Oliveira[9], Jacco Th. van Loon[9], Logan Francis[5], Jennifer Wiseman[1], Remy Indebetouw[10,11], C.-H. Rosie Chen[12], Roya Hamedani Golshan[13], and Danna Qasim[14]
[1] Exoplanets and Stellar Astrophysics Laboratory, NASA Goddard Space Flight Center, Greenbelt, MD 20771, USA; marta.m.sewilo@nasa.gov
[2] Department of Astronomy, University of Maryland, College Park, MD 20742, USA
[3] Center for Research and Exploration in Space Science and Technology, NASA Goddard Space Flight Center, Greenbelt, MD 20771, USA
[4] Laboratory for Astrophysics, Leiden Observatory, Leiden University, PO Box 9513, NL 2300 RA Leiden, The Netherlands
[5] Leiden Observatory, Leiden University, PO Box 9513, NL 2300 RA Leiden, The Netherlands
[6] INAF—Osservatorio Astronomico di Roma, Via di Frascati 33, 00078 Monte Porzio Catone, Italy
[7] Astrochemistry Laboratory, NASA Goddard Space Flight Center, Greenbelt, MD 20771, USA
[8] Department of Physics, Catholic University of America, Washington, DC 20064, USA
[9] Lennard-Jones Laboratories, Keele University, ST5 5BG, UK
[10] Department of Astronomy, University of Virginia, PO Box 400325, Charlottesville, VA 22904, USA
[11] National Radio Astronomy Observatory, 520 Edgemont Rd., Charlottesville, VA 22903, USA
[12] Max-Planck-Institut für Radioastronomie, Auf dem Hügel 69, D-53121 Bonn, Germany
[13] I. Physikalisches Institut der Universität zu Köln, Zülpicher Str. 77, 50937, Köln, Germany
[14] Southwest Research Institute, 6220 Culebra Rd., San Antonio, TX 78238, USA
Received 2025 June 30; revised 2025 September 19; accepted 2025 September 24; published 2025 October 20

Abstract

We present the results of James Webb Space Telescope observations of the protostar ST6 in the Large Magellanic Cloud (LMC) with the Medium Resolution Spectrograph of the Mid-Infrared Instrument (4.9–27.9 μm). Characterized by one-third to half-solar metallicity and strong UV radiation fields, the environment of the LMC allows us to study the physics and chemistry of star-forming regions under conditions similar to those at earlier cosmological epochs. We detected five icy complex organic molecules (COMs): methanol (CH_3OH), acetaldehyde (CH_3CHO), ethanol (CH_3CH_2OH), methyl formate ($HCOOCH_3$), and acetic acid (CH_3COOH). This is the first conclusive detection of CH_3COOH ice in an astrophysical context, and CH_3CHO, CH_3CH_2OH, and $HCOOCH_3$ ices are the first secure detections outside the Galaxy and in a low-metallicity environment. We address the presence of glycolaldehyde ($HOCH_2CHO$, a precursor of biomolecules), an isomer of $HCOOCH_3$ and CH_3COOH, but its detection is inconclusive. ST6's spectrum is also rich in simple ices: H_2O, CO_2, CH_4, SO_2, H_2CO, HCOOH, OCN^-, $HCOO^-$, NH_3, and NH_4^+. We obtain the composition and molecular abundances in the icy dust mantles by fitting the spectrum in the 6.8–8.4 μm range with a large sample of laboratory ice spectra using the ENIIGMA fitting tool or the local continuum method. We found differences in the simple and COM ice abundances with respect to H_2O ice between ST6 and Galactic protostars that likely reflect differences in metallicity and UV flux. More laboratory ice spectra of COMs are needed to better reconstruct the observed infrared spectra of protostars.

Unified Astronomy Thesaurus concepts: Star formation (1569); Astrochemistry (75); Magellanic Clouds (990); Chemical abundances (224); Protostars (1302); Infrared spectroscopy (2285); Ice composition (2272)

1. Introduction

Complex organic molecules (COMs; carbon-bearing molecules with at least six atoms; e.g., E. Herbst & E. F. van Dishoeck 2009), including those considered as precursors of prebiotic species, have been detected in the gas phase at each stage of star formation—from cold prestellar cores to hot regions surrounding low- and high-mass protostars (hot cores and hot corinos) and protoplanetary disks (e.g., J. K. Jørgensen et al. 2020 and references therein). Identifying the formation and destruction routes of COMs is therefore crucial for our understanding of the star and planet formation process. COMs can be formed both in the gas and on the surfaces of interstellar dust grains (e.g., E. Herbst & E. F. van Dishoeck 2009; A. C. A. Boogert et al. 2015; K. I. Öberg 2016; K. I. Öberg & E. A. Bergin 2021). As indicated by chemical models and laboratory experiments, grain-surface chemistry is the main contributor to their production (e.g., R. T. Garrod et al. 2022).

While the number of detected gas-phase COMs has been rising steadily (e.g., B. A. McGuire 2022), evidence for the presence of COMs in the solid state was lacking until the launch of the James Webb Space Telescope (JWST; J. P. Gardner et al. 2023; J. Rigby et al. 2023). Pre-JWST, CH_3OH was the only COM securely detected in ices toward Galactic sources (e.g., A. C. A. Boogert et al. 2015). Recent JWST observations with the Medium Resolution Spectrograph (MRS; M. Wells et al. 2015; A. Labiano et al. 2021; I. Argyriou et al. 2023) of the Mid-Infrared Instrument (MIRI; G. S. Wright et al. 2023) of two low-mass and two high-mass Galactic protostars resulted in the detection of several COM ices other than CH_3OH (Y. Chen et al. 2024; W. R. M. Rocha et al. 2024b; E. F. van Dishoeck et al. 2025; see Section 4.2): acetaldehyde (CH_3CHO), ethanol (CH_3CH_2OH), methyl formate ($HCOOCH_3$), dimethyl ether

Original content from this work may be used under the terms of the Creative Commons Attribution 4.0 licence. Any further distribution of this work must maintain attribution to the author(s) and the title of the work, journal citation and DOI.

(CH_3OCH_3), and, tentatively, acetic acid (CH_3COOH). The presence of these species in ices provides evidence for them being the products of grain-surface chemistry.

The Large Magellanic Cloud (LMC), the nearest star-forming satellite of the Milky Way, provides us with an opportunity to investigate COMs in both gas and ice in a distinct environment from that in our galaxy. The LMC's environment is characterized by subsolar metallicity ($Z_{LMC} = 0.3$–$0.5\ Z_\odot$; e.g., S. C. Russell & M. A. Dopita 1992; L. Toribio San Cipriano et al. 2017) and strong ultraviolet (UV) radiation fields (e.g., M. K. Browning et al. 2003; D. E. Welty et al. 2006). The relatively small distance of the LMC of ∼50 kpc (G. Pietrzyński et al. 2019) allows us to resolve individual protostars with instruments such as the Atacama Large Millimeter/submillimeter Array (ALMA) and JWST and study COMs in the gas (ALMA) and ice (JWST).

There are several factors that can directly impact the formation and survival of COMs in a low-metallicity environment. The abundance of atomic C, O, and N atoms in the LMC is lower when compared with the Galaxy (i.e., fewer C, O, and N atoms are available for chemistry; e.g., S. C. Russell & M. A. Dopita 1992). The dust-to-gas ratio in the LMC is lower (e.g., J. Roman-Duval et al. 2014), resulting in fewer dust grains for surface chemistry and less shielding than in the Galaxy. The deficiency of dust combined with the harsher UV radiation field in the LMC (e.g., M. K. Browning et al. 2003; D. E. Welty et al. 2006) leads to warmer dust temperatures (e.g., J. T. van Loon et al. 2010a, 2010b; J. M. Oliveira et al. 2019) and, consequently, less efficient grain-surface reactions (e.g., K. Acharyya & E. Herbst 2015; T. Shimonishi et al. 2016a). The LMC's cosmic-ray density is about 25% of that measured in the solar neighborhood (e.g., A. A. Abdo et al. 2010), resulting in less effective cosmic-ray-induced UV radiation.

To date, only a handful of gas-phase COMs larger than CH_3OH have been securely detected in LMC hot cores with ALMA (M. Sewiło et al. 2018, 2019, 2022, and 2026, in preparation; T. Shimonishi et al. 2020; R. Hamedani Golshan et al. 2024; A. Broadmeadow et al. 2025): methyl formate ($HCOOCH_3$), dimethyl ether (CH_3OCH_3), and methyl cyanide (CH_3CN). The tentative detection has been reported for the astrobiologically relevant formamide (NH_2CHO; M. Sewiło et al. 2022). Even though only 10 hot cores are known in the LMC, they show a surprisingly large chemical diversity that is not yet understood. Interestingly, cold gas-phase methanol emission (both compact and extended) is widespread in the LMC (e.g., R. Hamedani Golshan et al. 2024).

Low spectral resolution near- and mid-IR studies on ices in the LMC (J. T. van Loon et al. 2005; J. M. Oliveira et al. 2006, 2009, 2011; T. Shimonishi et al. 2008, 2010, 2016a; J. P. Seale et al. 2009, 2011) revealed differences in relative ice abundances and thermal processing levels of the simplest ices (H_2O, CO_2, and CO) between the LMC and Galactic young stellar objects (YSOs). On average, the CO_2-to-H_2O ice column density ratio is about 2 times higher in the LMC than in the Galaxy, while the CO-to-H_2O ice column density ratio is comparable (T. Shimonishi et al. 2016a and references therein). The overabundance of CO_2 ice can be explained by the combined effects of the stronger UV radiation field and the higher dust temperature in the LMC compared to the Galaxy. J. M. Oliveira et al. (2011) proposed that the larger CO_2/H_2O ice ratio in the LMC may be the result of the underabundance of H_2O ice rather than the overabundance of CO_2 ice. The detailed analysis of the 15.2 μm CO_2 ice absorption band led J. M. Oliveira et al. (2009) and J. P. Seale et al. (2011) to the conclusion that the CO_2 ices around the LMC massive YSOs may be more thermally processed than those in Galactic YSOs.

JWST has enabled studies of ice chemistry in the LMC with high sensitivity and spectral resolution, allowing for a reliable identification and detailed analysis of ice band profiles, and on spatial scales matching the gas-phase observations of COMs. We used the Near Infrared Spectrograph (NIRSpec) integral field unit (IFU; M. F. Closs et al. 2008; T. Böker et al. 2022) and MIRI MRS to map the near-IR (2.87–5.27 μm) and mid-IR (4.9–27.9 μm) ice content in the envelopes of two protostars in the low-metallicity LMC: ST6 and N 83A–mm A. ST6 (T. Shimonishi et al. 2008; 053941.12−692916.8 in R. A. Gruendl & Y. Chu 2009; L. R. Carlson et al. 2012) and N 83A–mm A (045400.10−691155.5 in R. A. Gruendl & Y. Chu 2009; #90 in B. A. Whitney et al. 2008) were selected from a small sample of LMC sources with a reported detection (reliable or marginal) of COMs in the gas with ALMA (T. Shimonishi et al. 2016b, 2021; M. Sewiło et al. 2018, 2019, 2022; R. Hamedani Golshan et al. 2024). ST6 is a deeply embedded massive protostar in the star-forming region N158, ∼25″ south of 30 Doradus (see Figure 1 and Appendix A). Slightly more evolved N 83A–mm A is a hot core located in the star-forming region N83 in the southwestern part of the LMC (M. Sewiło et al. 2026, in preparation). Here, we present the results of the MIRI MRS observations of ST6, concentrating on the spectral region between 6.8 and 8.4 μm covering the main ice features associated with COMs ("ice COMs region"; e.g., W. R. M. Rocha et al. 2024b and references therein).

In Section 2, we provide information on the JWST observations of ST6 and the MIRI MRS data processing. In Section 3, we describe the spectral analysis and ice column density determination. We discuss the results in Section 4 and provide conclusions in Section 5.

2. JWST Observations

The JWST observations were carried out as part of the General Observer (GO) Cycle 2 Program 3702 (PI: M. Sewiło). The MIRI MRS observations of ST6 were conducted on 2024 March 10. The observations were carried out in the FASTR1 detector readout mode using all four IFU sets (channels 1–4) with all three grating settings (subbands *A*, *B*, and *C*), providing full wavelength coverage between 4.9 and 27.9 μm. Channel (1, 2, 3, 4) covers a wavelength range of (4.9–7.65, 7.51–11.7, 11.55–17.98, 17.7–27.9) μm and has a field of view of ($3\farcs3 \times 3\farcs7$, $4\farcs0 \times 4\farcs8$, $5\farcs2 \times 6\farcs2$, $6\farcs6 \times 7\farcs7$). The spectral resolving power changes between the MRS subbands, ranging from ∼3500 at 5 μm to ∼1500 at 28 μm. The four-point extended source dithering pattern was used for the MRS, as it maximizes the common field of view between different pointings while still obtaining good sampling. The on-source integration time in each grating was 1287.6 s, resulting in a total integration time of 64.4 minutes. The MIRI MRS observations were associated with dedicated background observations with the same settings, which were executed in a noninterruptible sequence.

The MIRI MRS observations were processed through the JWST calibration pipeline version 1.13.4 (H. Bushouse et al. 2024) using the reference context `jwst_1231.pmap` of the JWST Calibration Reference Data System (P. Greenfield &

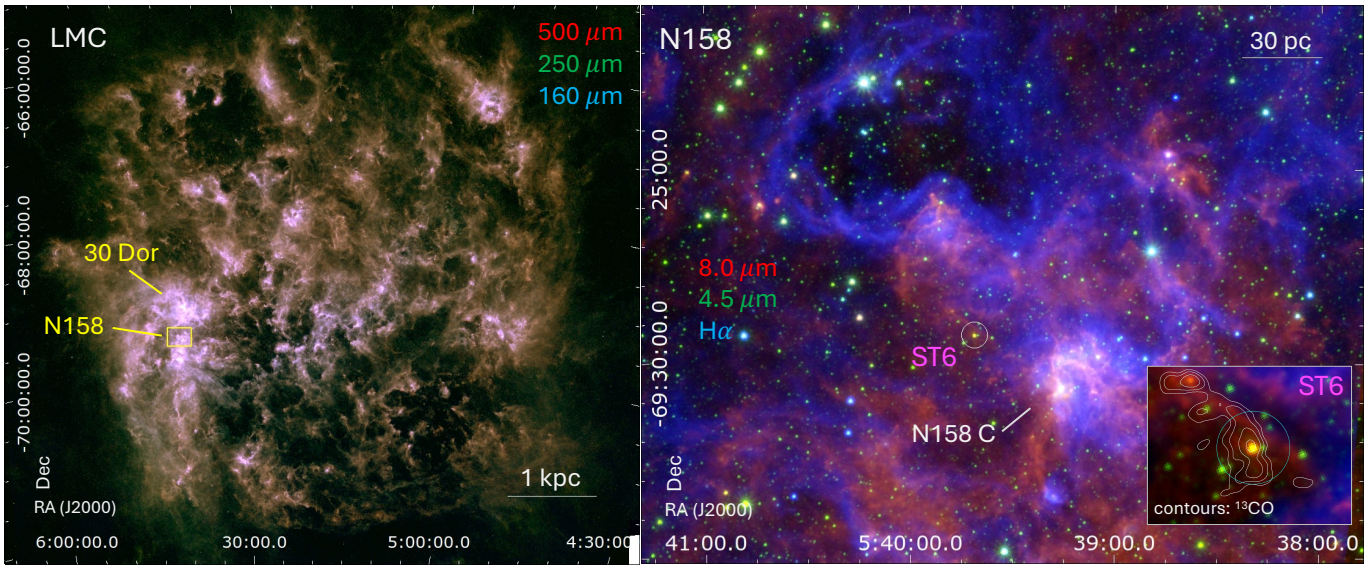


Figure 1. The left panel shows the three-color mosaic of the LMC combining Herschel/HERITAGE SPIRE 500 μm (red) and 250 μm (green) and PACS 160 μm (blue; M. Meixner et al. 2013) images with the positions of star-forming regions N158 (hosting ST6) and 30 Dor indicated. The yellow rectangle outlines the field of view of the image shown in the right panel: a three-color mosaic of N158, combining Spitzer/SAGE IRAC 8.0 μm (red), 4.5 μm (green; M. Meixner et al. 2006), and MCELS Hα (blue; R. C. Smith & MCELS Team 1998) images. The position of ST6 is indicated with a white circle and labeled. The inset shows a zoom-in on ST6 and its surroundings. The contours represent the ^{13}CO (2–1) emission with contour levels of (10, 20, 40, 80)% of the emission peak of 12.4 Jy beam^{-1} km s^{-1}; the synthesized beam size is $7'' \times 7''$. See Appendix A for more details.

T. Miller 2016). First, the raw data were processed through the `Detector1Pipeline` using the default settings (stage 1). The `Spec2Pipeline` was run in the subsequent stage 2; it included fringe correction using a fringe flat field derived from spatially extended sources and detector-level residual fringe correction. The background was subtracted from the science data using the rate files of the dedicated background after masking bright emission lines, so that no real astronomical features are removed. A bad-pixel routine was applied to the `Spec2Pipeline` data products outside of the default MIRI MRS pipeline using the Vortex Image Processing package (V. Christiaens et al. 2023). In stage 3, the `Spec3Pipeline` was executed with the master background and outlier rejection routines turned off, the former due to the background being already subtracted and the latter because it did not significantly improve the quality of the data. The `Spec3Pipeline` produced data cubes for each band of each channel separately.

The MIRI MRS spectrum of ST6 was extracted from the circular wavelength-dependent aperture centered on its mid-IR continuum peak at the ICRS (J2000) coordinates of (R.A., decl.) = ($05^{h}39^{m}41\overset{s}{.}121$, $-69°29'16\overset{''}{.}80$). We used the aperture with a diameter of $3 \times \mathrm{FWHM_{PSF}}$, where $\mathrm{FWHM_{PSF}}$ is the empirically derived full width at half-maximum (FWHM) of the MIRI MRS point-spread function (PSF) at a given wavelength (λ): $\mathrm{FWHM_{PSF}} = 0.033(\lambda/\mu\mathrm{m}) + 0\overset{''}{.}106$ (D. R. Law et al. 2023). The adopted size of the aperture ensures that we capture as much of the emission from ST6 as possible without significant contamination from the environment, specifically from polycyclic aromatic hydrocarbon (PAH) emission. Example MIRI MRS channel maps with the spectral extraction apertures overlaid are shown in Figure B1 in Appendix B. MIRI's spatial resolution ($\mathrm{FWHM_{PSF}}$) of ($0\overset{''}{.}27$, $0\overset{''}{.}44$, $0\overset{''}{.}60$) at (5, 10, 15) μm corresponds to (0.066, 0.106, 0.146) pc or ~(13,600, 21,900, 30,100) au at 50 kpc.

We applied a 1D residual fringe correction to the extracted spectrum of ST6 using the pipeline routine `fit_residual_fringes_1d` to remove residual periodic fringes (I. Argyriou et al. 2020). Next, the spectra from individual subbands were stitched (matched in flux) in order of increasing wavelength using the channel 1A spectrum as a base spectrum to form a continuous spectrum between 4.9 and ~29 μm. For the overlapping wavelengths, the part of the already stitched spectrum was kept. The flux offsets between consecutive bands were very small (1%–2%); thus, the stitching procedure does not affect the shape and optical depth of the absorption features. The resulting MIRI MRS spectrum of ST6 is shown in Figure 2. Doppler correction has been applied to the spectrum before the ice analysis. A velocity of 227 km s^{-1} was measured based on the H_2O gas lines.

3. The Analysis and Results

In our spectral analysis, we follow the procedure outlined in W. R. M. Rocha et al. (2024b). We perform global continuum subtraction and silicate removal from the spectrum of ST6 (with the emission lines masked), followed by local continuum subtraction around the 6.8–8.4 μm wavelength range, the ice COM fingerprint region. Then, we identify the COM and simple ice species detected toward ST6 and determine their column densities.

3.1. The Global Continuum and Silicate Subtraction

We determined the global continuum using an iterative process that included several steps: (1) selecting an initial global continuum by fitting a polynomial function to a set of guiding points and deriving the optical depth spectrum, (2) matching a synthetic silicate model to the global-continuum-subtracted spectrum, (3) finding a H_2O model best matching the global continuum and silicate-subtracted spectrum, and (4) adjusting the guiding points and repeating the process until identifying the combination of silicate and H_2O models best reproducing the observed spectrum.

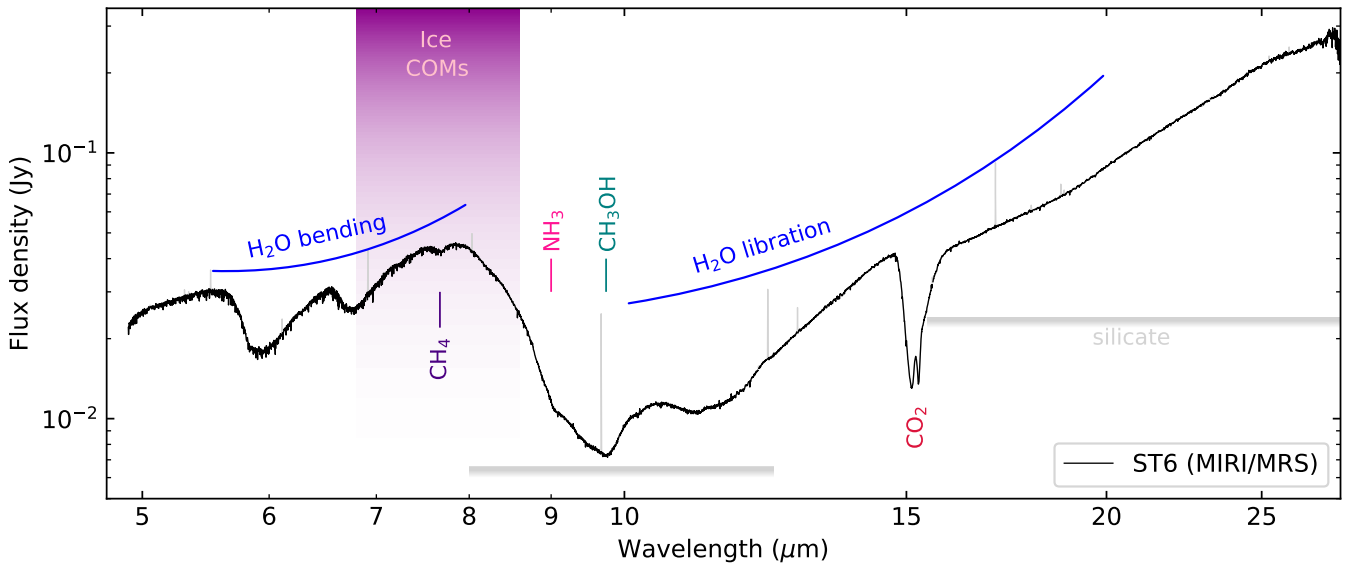


Figure 2. The JWST MIRI MRS spectrum of the massive protostar ST6 in the LMC. The gas-phase emission lines (shown in gray) are masked for the ice analysis. Gas-phase absorption lines remain in the spectrum. In this work, we concentrate on the spectral region between 6.8 and 8.4 μm (indicated in purple) covering the main ice features associated with COMs. Major ice and silicate (9.7 and 18 μm) features are indicated.

Due to the presence of the broad ice and silicate features in the spectrum of ST6, only a narrow wavelength range can be considered as continuum-only (5.3–5.5 μm). Thus, the positions of the guiding points at longer wavelengths were selected to account for the presence of these features. We determined the final global continuum by fitting a polynomial of the fourth order to a set of guiding points shown in Figure B2(a). The resulting global continuum (the polynomial fit) overlaid on the spectrum of ST6 is also presented in Figure B2(a).

Next, we derived the optical depth spectrum using the relation

$$\tau_\lambda = -\ln\left(\frac{F_\lambda^{\rm source}}{F_\lambda^{\rm cont}}\right), \quad (1)$$

where τ_λ is the optical depth at wavelength λ, $F_\lambda^{\rm source}$ is the observed spectrum (with the emission lines masked), and $F_\lambda^{\rm cont}$ is the continuum.

The optical depth spectrum of ST6 reveals a significant contribution from the silicate features at 9.8 and 18 μm that must be removed before the analysis of the absorption features attributed to icy molecules. To find the silicate profile best matching the shape of the silicate features in the spectrum of ST6, we considered the mixtures of synthetic amorphous pyroxene ($Mg_{0.7}Fe_{0.3}SiO_3$) and olivine ($MgFeSiO_4$; J. Dorschner et al. 1995), polivene ($Mg_{1.5}SiO_{3.5}$, silicate dust with stoichiometry intermediate between olivine and pyroxene; C. Jäger et al. 2003; S. Fogerty et al. 2016), and the observed silicate profile of the Galactic Center source GCS 3 used in the literature as a silicate feature template (e.g., F. Kemper et al. 2004; S. Bottinelli et al. 2010). Previous JWST MIRI MRS papers (M. K. McClure et al. 2023; W. R. M. Rocha et al. 2024b) used a combination of pyroxene and olivine motivated by A. C. A. Boogert et al. (2013). However, in the case of ST6, we found a better spectral fit using polivene instead of olivine. Polivene was first used by S. Fogerty et al. (2016) to fit the dust emission spectral profile of protoplanetary disks. The synthetic silicate profile best matching the spectrum of ST6 is shown in Figure B2(b); it is a combination of the amorphous pyroxene and polivene spectra, with the absorption of pyroxene dominating over polivene. The global continuum and silicate-subtracted optical depth spectrum of ST6 is presented in Figure B2(c). The rms noise level in the spectrum is 0.004 based on the measurements in the 9.94–10.06 μm and 15.34–15.43 μm wavelength ranges.

Lastly, we compared ST6's global continuum and silicate-subtracted spectrum to the H_2O ice synthetic spectra. In the MIRI MRS spectrum of ST6, two prominent H_2O ice bands are present: the O–H bending mode (ν_2) at 6 μm and the libration mode at 13.2 μm. To determine the contribution of H_2O ice, we compared ST6's spectrum to the H_2O ice synthetic spectra for different temperatures, single grain sizes or grain distributions, and grain geometries. The combination of two H_2O ice models with temperatures of 10 and 160 K provides the best match to the data. Both models use the Mie approach (perfectly spherical grains; G. Mie 1908) and a single grain size of 0.1 μm. The lower-temperature (10 K) model is adopted from A. C. A. Boogert et al. (2008). We used the `optool` code (C. Dominik et al. 2021) to derive H_2O ice opacities for a temperature of 160 K utilizing the optical constants from W. R. M. Rocha et al. (2024a) and assuming that the ice mantle is composed of pure H_2O ice. The best-matching H_2O synthetic spectrum is overlaid on the global continuum and silicate-subtracted spectrum of ST6 in Figure B2(c).

3.2. Spectral Modeling with the ENIIGMA Fitting Tool: 6.8–8.4 μm

We used the `ENIIGMA` fitting tool (W. R. M. Rocha et al. 2021) to simultaneously fit ice features in the COMs region of ST6's spectrum with laboratory data representing realistic ice mixtures measured at relevant astrophysical temperatures.

`ENIIGMA` is a Python tool that performs spectral fitting using genetic modeling algorithms and statistical analysis of the solution. The model is defined as a linear combination of the laboratory spectrum ($\tau_\nu^{\rm lab}$), where the coefficients vary to fit the observational data ($\tau_\nu^{\rm obs}$). We adopted the rms error

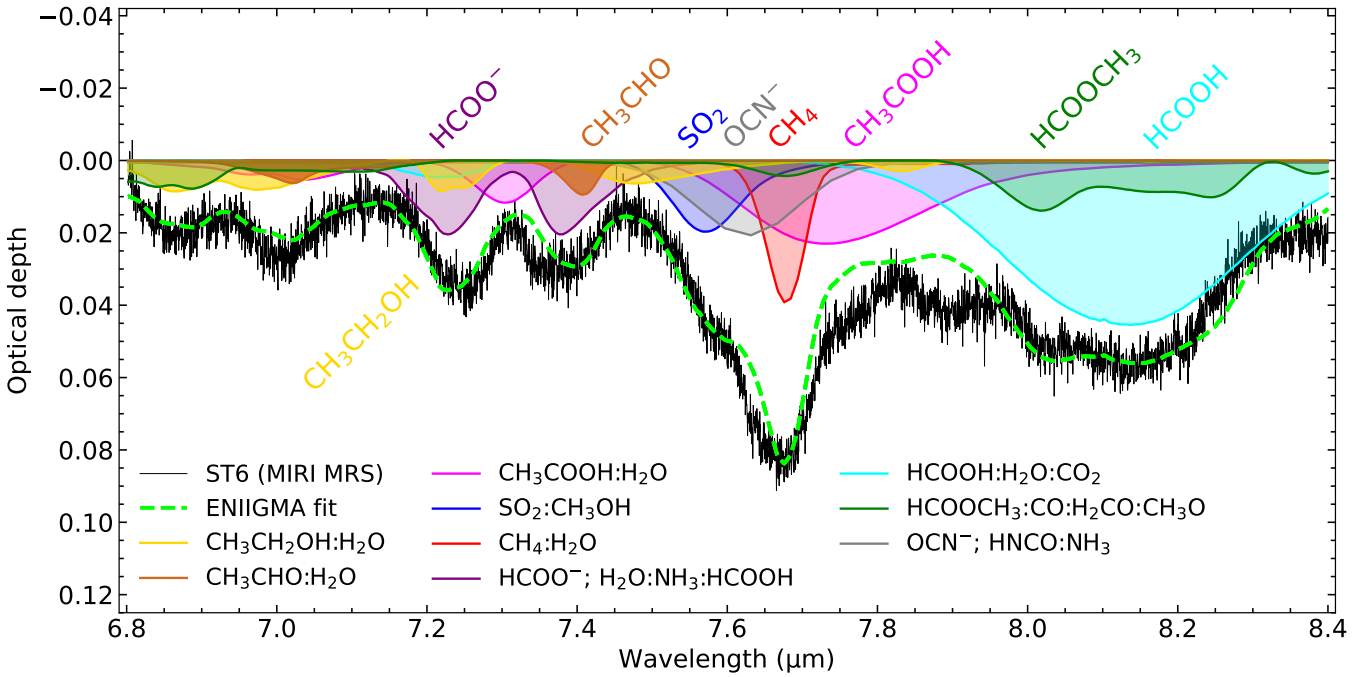


Figure 3. The ENIIGMA fit to the MIRI MRS spectrum of ST6 in the 6.8–8.4 μm wavelength range. The ice mixtures used in the fit are listed in the legend. The name of each detected ice species is also indicated in the plot in the corresponding color.

(RMSE) as the fitness function, defined as

$$\mathrm{RMSE} = \sqrt{\frac{1}{n}\sum_{i=0}^{n-1}\left(\tau_{\nu,i}^{\mathrm{obs}} - \sum_{j=0}^{m-1} w_j \tau_{\nu,j}^{\mathrm{lab}}\right)^2}, \quad (2)$$

where both $\tau_{\nu,\mathrm{j}}^{\mathrm{lab}}$ and $\tau_{\nu,\mathrm{i}}^{\mathrm{obs}}$ are converted to wavenumber space (ν), w_j is the scale factor, and m and n are the m^{th} and n^{th} data points.

The statistical analysis consists of determining the confidence intervals of each ice component of the spectral decomposition, which are calculated based on the $\Delta\chi^2$ map (Y. Avni & J. N. Bahcall 1980). Here, we perform a perturbation around those coefficients providing the best fit. With the new models, a large sample of new χ^2 values is calculated, which are compared with the best-fit χ^2_{min}.

To prepare the spectrum of ST6 for ENIIGMA fitting, we first removed gas-phase absorption lines mostly due to H_2O as described in Appendix C. Next, we performed a local continuum subtraction as illustrated in Figure B3 (see also Figure B4). This procedure accounts for the contribution of broad features not included in the fit, such as the H_2O ice bending mode and possibly organic refractory material (E. L. Gibb & D. C. B. Whittet 2002; A. C. A. Boogert et al. 2008; A. Potapov et al. 2025). The nature of the remaining inflexions in the spectrum is investigated with the ENIIGMA fitting tool. The laboratory data used to fit the spectrum of ST6 are listed in Table 2 in Appendix C. The full ENIIGMA fit is shown in Figure 3, while the individual components are displayed in Figure C1.

3.3. Inventory of COM and Simple Ices toward ST6

We detected CH_3OH, CH_3CHO, CH_3CH_2OH, $HCOOCH_3$, and CH_3COOH ices toward ST6. The detection of CH_3COOH ice constitutes the first conclusive detection of this icy species, while CH_3CHO, CH_3CH_2OH, and $HCOOCH_3$ ices are observed for the first time outside the Galaxy and in a low-metallicity environment.

With the exception of CH_3OH, these COMs were identified with ENIIGMA by fitting the 6.8–8.4 μm spectral range (see Figures 3 and C1); each species has at least two transitions detected with a statistical significance of 3σ. For CH_3OH, the ice absorption features were identified and analyzed using the local continuum method.

Two CH_3OH ice absorption features have been detected toward ST6 with JWST: the C–O stretching mode at 9.74 μm (MIRI MRS; see Table 1 and Appendix E) and the C–H stretching mode at 3.53 μm (NIRSpec IFU; see Appendix D).

In addition to COM ices, we detected simple ices toward ST6: H_2O, CO_2, CH_4, SO_2, NH_3, H_2CO, HCOOH, $HCOO^-$, NH_4^+, and OCN^-, as presented in Figure 3 and Appendix E; see also Table 1 for a list of detected transitions utilized in the further analysis. H_2O has two distinct ice bands across the MIRI MRS spectrum at 6 and 13.2 μm, and CO_2 at 15.2 μm. CH_4 has a clear band at 7.67 μm, whereas SO_2 and OCN^- together contribute to the red wing of that band. $HCOO^-$ shows a clear contribution to the 7.2 and 7.4 μm bands, characteristic of embedded protostars. Its precursor, HCOOH, is clearly visible at 8.2 μm, near the H_2CO band at 8 μm. Finally, NH_3 is identified via the broad umbrella mode at 9 μm.

3.4. Determination of Ice Column Densities

We utilize the COM and simple ice bands listed in Table 1 to determine ice column densities (N_{ice}) toward ST6 using the formula

$$N_{\mathrm{ice}} = \frac{1}{A}\int_{\nu_1}^{\nu_2} \tau_\nu \, d\nu, \quad (3)$$

where τ is the optical depth, ν is the wavenumber (in units of cm^{-1}), and A is the band strength of a given ice feature measured in the laboratory (cm $\mathrm{molecule}^{-1}$; provided in Table 1). When the absorption feature of the targeted species is

Table 1
Transitions of the Detected Species Used for Ice Column Density Determination and the Results

Species, X[a]	λ (μm)	ν (cm^{-1})	Identification	Band Strength[b] (cm molecule^{-1})	Ref.	N_{ice}(X) (10^{17} cm^{-2})	N_{ice}(X)/N_{ice}(H_2O) (%)
						ENIIGMA Fitting	
CH_4	7.67	1303	CH_4 def.	8.4×10^{-18}	1	$0.52^{+0.10}_{-0.06}$	$0.46^{+0.13}_{-0.11}$
SO_2	7.60	1320	SO_2 stretch	3.4×10^{-17}	2	$0.11^{+0.02}_{-0.02}$	$0.10^{+0.03}_{-0.03}$
H_2CO	8.04	1244	CH_2 rock	1.0×10^{-18}	1	$0.24^{+0.10}_{-0.07}$	$0.22^{+0.10}_{-0.07}$
HCOOH	8.22	1216	C–O stretch	2.9×10^{-17}	1	$0.83^{+0.14}_{-0.22}$	$0.74^{+0.19}_{-0.25}$
CH_3CHO	7.41	1349	CH_3 s-def./CH wag.	4.1×10^{-18}[b]	3	$0.26^{+0.10}_{-0.09}$	$0.23^{+0.10}_{-0.09}$
CH_3CH_2OH	7.23	1383	CH_3 s-def.	2.4×10^{-18}[b]	4	$0.49^{+0.15}_{-0.15}$	$0.43^{+0.16}_{-0.16}$
$HCOOCH_3$	8.25	1211	C–O stretch	2.28×10^{-17}[b]	5	$0.11^{+0.04}_{-0.03}$	$0.096^{+0.043}_{-0.033}$
CH_3COOH	7.82	1278	OH bend	4.57×10^{-17}	6	$0.26^{+0.05}_{-0.03}$	$0.23^{+0.06}_{-0.05}$
OCN^-	7.62	1312	Comb. ($2\nu_2$)	7.45×10^{-18}	6	$0.86^{+0.14}_{-0.09}$	$0.76^{+0.19}_{-0.17}$
$HCOO^-$	7.38	1355	C–O stretch	1.7×10^{-17}	7	$0.27^{+0.13}_{-0.15}$	$0.23^{+0.12}_{-0.14}$
						Local Continuum Method	
H_2O	13.20	760	Libration	3.2×10^{-17}	1	113 ± 23	100
NH_3	9.0	1111	NH str.	2.1×10^{-17}	1	3.78 ± 0.76	3.35 ± 0.95
CO_2	15.27	654.7	Bend	$(1.73 \pm 0.53) \times 10^{-17}$	8	24.7 ± 7.6	21.9 ± 8.0
CH_3OH	9.74	1026	C–O stretch	1.62×10^{-17}	9	2.76 ± 0.15	2.45 ± 0.51
NH_4^+	6.85	1460	NH_4^+ bend	$(3.2 \pm 0.3) \times 10^{-17}$	10	5.74 ± 0.13	5.09 ± 1.03

Notes.
[a] The species are (from top to bottom): methane (CH_4), sulfur dioxide (SO_2), formaldehyde (H_2CO), formic acid (HCOOH), acetaldehyde (CH_3CHO), ethanol (CH_3CH_2OH), methyl formate ($HCOOCH_3$), acetic acid (CH_3COOH), cyanate ion (OCN^-), formate ion ($HCOO^-$), water (H_2O), ammonia (NH_3), carbon dioxide (CO_2), methanol (CH_3OH), and ammonium (NH_4^+).
[b] We provide band strengths for a specific ice mixture used for the ENIIGMA fitting for species with the band strength correction available in the literature: CH_3CHO, CH_3CH_2OH, and $HCOOCH_3$. No correction is required for ions. See Section 3.4 and Table 2 for details.
References. (1) M. Bouilloud et al. (2015); (2) A. C. A. Boogert et al. (1997); (3) R. L. Hudson & R. F. Ferrante (2020); (4) N. Boudin et al. (1998); (5) J. Terwisscha van Scheltinga et al. (2021); (6) W. R. M. Rocha et al. (2024b); (7) W. A. Schutte et al. (1999); (8) P. A. Gerakines & R. L. Hudson (2015); (9) R. L. Hudson et al. (2024); (10) K. Slavicinska et al. (2025a).

blended with those from other molecules, we first isolate the feature of our interest before calculating N_{ice}.

The band strength is a molecular property that depends on the ice structure (amorphous, crystalline) and composition (pure, mixed). To account for its dependence on the chemical environment, we use band strengths for the specific ice mixtures used in the ENIIGMA fitting for all the species with the band strength correction available in the literature, i.e., CH_3CHO, CH_3CH_2OH, and $HCOOCH_3$ (J. Terwisscha van Scheltinga et al. 2018, 2021; see Table 1). The band strength correction is calculated as a ratio of the integrated area of a specific band in a mixture and that of the pure ice. No correction is required for ions (OCN^-, $HCOO^-$, and NH_4^+), as band strengths are determined for specific mixtures. Ions are naturally formed via acid–base reactions from other species; they do not exist in the pure ice but are part of a set of species that exist together with other ions. For the remaining species, we adopt the band strengths of the pure ice.

The resulting N_{ice} and ice abundances with respect to H_2O ice for each species (X), $N_{X,ice}/N_{H_2O,\,ice}$, are listed in Table 1. The $N_{X,ice}/N_{H_2O,\,ice}$ ratios are presented graphically in a bar plot in Figure 4, where they are compared to those measured toward the four Galactic protostars with the detection of COM ices (see the discussion in Section 4.2). More details on N_{ice} calculations are provided in Sections 3.4.1 and 3.4.2 for COM and simple ices, respectively.

3.4.1. Column Densities of COM Ices

Isolated and not significantly blended bands are most suitable for ice column density calculations; however, they are often unavailable for COM ices. For blended ice absorption bands, ENIIGMA is used to determine the optimal intensities of the overlapping features.

In the 6.8–8.4 μm wavelength range, the bands of CH_3CH_2OH at 7.2 μm and CH_3CHO at 7.4 μm are adopted in the ice column density calculations for these two species (see Table 1). CH_3COOH and $HCOOCH_3$, two isomers, are constrained based on the transitions at 7.82 and 8.25 μm, respectively.

To determine the CH_3OH ice column density, we utilized the isolated feature at 9.7 μm. This feature lies outside the ENIIGMA fitting range (our main spectral region of interest in this work); thus, its ice column density was determined based on the local continuum method. We performed the local continuum subtraction in the ~8.6–10.1 μm spectral range that covers both the CH_3OH 9.7 μm ice band and the nearby NH_3 ice band at 9 μm to best capture the shape of both features.

The CH_3OH and NH_3 ice bands in the silicate-subtracted spectrum of ST6 were isolated before integration by fitting a second-order polynomial to the guiding points tracing the local continuum as illustrated in Figure E1 in Appendix E. To determine the CH_3OH ice column density, we integrated the 9.7 μm band in the local-continuum-subtracted spectrum between 9.45 and 10.08 μm. The selection of the local continuum results in an uncertainty of ~10% in integrated optical depth. The determination of the NH_3 ice column density is described in Section 3.4.2.

The column densities of COM ices are provided in Table 1. For all COMs except CH_3OH (i.e., those with N_{ice} determined with ENIIGMA), the uncertainties are determined from the

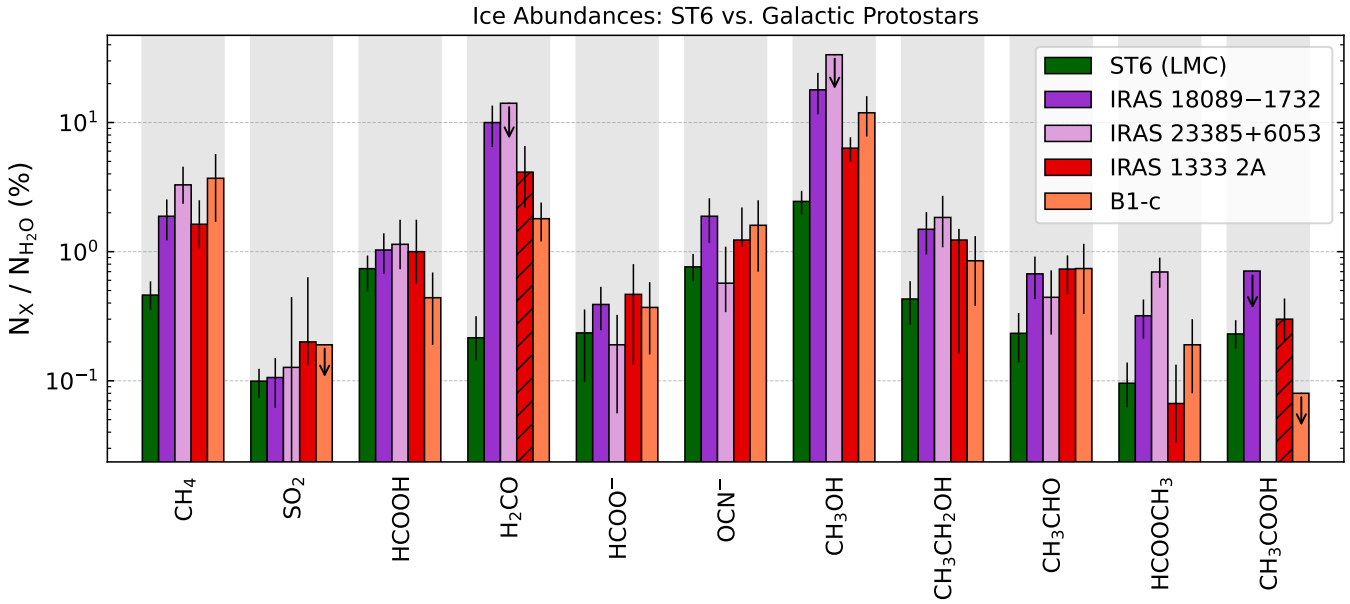


Figure 4. Ice abundances with respect to H_2O ice of ST6 compared to those of Galactic protostars with large COM ice detections: the high-mass protostars IRAS 23385 (W. R. M. Rocha et al. 2024b) and IRAS 18089 (E. F. van Dishoeck et al. 2025) and low-mass protostars (hot corinos) IRAS 2A (Y. Chen et al. 2024; W. R. M. Rocha et al. 2024b) and B1–c (Y. Chen et al. 2024). The ice abundances for IRAS 2A are from W. R. M. Rocha et al. (2024b). The 13.2 μm H_2O band was used to determine $N_{H_2O,\,ice}$ for all the sources. The hatches and arrows indicate tentative detections and upper limits, respectively.

confidence interval analysis based on the $\Delta\chi^2$ maps within the 3σ level of significance (see W. R. M. Rocha et al. 2021). For CH_3OH, the ice column density uncertainties were estimated by error propagation. The uncertainty of the integrated optical depth was determined using a per-channel rms, assuming that each spectral resolution element is an independent measurement. R. L. Hudson et al. (2024) provide the band strength uncertainty of 5% for the CH_3OH 9.7 μm ice band.

3.4.2. Column Densities of Simple Ices

For simple ices with isolated or relatively isolated features in the ENIIGMA fitting wavelength range (i.e., CH_4, SO_2, H_2CO, HCOOH, OCN^-, and $HCOO^-$; Table 1), we simply integrate the full bands and use Equation (3) to determine N_{ice}. For $HCOO^-$ that has two features between 6.8 and 8.4 μm, at 7.2 and 7.4 μm, we adopted the 7.4 μm band to avoid accounting for the HCOOH band at 7.2 μm that is the precursor of $HCOO^-$. For H_2CO that is present in the same mixture with $HCOOCH_3$, the 8.0 μm ice band is isolated by using a combination of Gaussian functions as described in W. R. M. Rocha et al. (2021). The uncertainties are derived from the confidence interval analysis (see above).

For simple ices with features used for the N_{ice} calculations at wavelengths outside the ENIIGMA fitting range (i.e., CO_2, NH_3, NH_4^+, and H_2O), we use the local continuum method. For CO_2 ice, we simply integrated the band at 15.2 μm after the local continuum subtraction (see Figure E1), whereas a few more steps were required for the remaining species.

The shape of the NH_3 ice absorption band at 9 μm indicates likely contributions from other species (see Figure E1). We identify three overlapping absorption ice features with no prior spectral assignment in the ~8.76–8.83 μm, ~8.84–8.93 μm, and ~8.99–9.08 μm wavelength ranges. In Section 4.5, we discuss a possible contribution from glycolaldehyde ($HOCH_2CHO$) to the latter two ice features. We approximate the shape of the local-continuum-subtracted NH_3 ice band by a double-peaked Gaussian function (shown in Figure E1), excluding the three overlying absorption features.

The CH_3 rocking band of CH_3OH at 8.86 μm (1129 cm^{-1}; R. L. Hudson et al. 2024) overlaps with the NH_3 ice band, and its contribution has to be taken into account when calculating $N_{NH_3,\,ice}$. We estimate the shape and intensity of the 8.86 μm CH_3OH ice band by scaling the laboratory spectrum of pure CH_3OH to match the intensity of the CH_3OH ice band at 9.74 μm (1026 cm^{-1}). We adopt the area under the double-peaked Gaussian function after subtracting the area of the CH_3OH rocking band (~5.3%) as the integrated optical depth of the NH_3 ice band in Equation (3).

The local continuum subtraction procedure for the 6.8 μm ice feature attributed to the ammonium (NH_4^+) bend with the contribution from the CH_3OH C–H reformation mode is illustrated in Figure E2. We obtain the NH_4^+ integrated optical depth from the local-continuum-subtracted spectrum by integrating the 6.8 μm ice band and removing the contribution from the CH_3OH C–H reformation mode. The contribution from the CH_3OH C–H deformation mode to the 6.8 μm ice band was estimated by integrating the CH_3OH laboratory spectrum (D. M. Hudgins et al. 1993) matched to the intensity of the CH_3OH ice band at 9.74 μm.

To determine $N_{H_2O,\,ice}$ using Equation (3), we perform a direct integration between 10 μm (1000 cm^{-1}) and 20 μm (500 cm^{-1}) of the H_2O ice two-temperature component model described in Section 3.1.

The CO_2, NH_3, NH_4^+, and H_2O ice column density uncertainties were estimated as described above for CH_3OH. The band strength uncertainties for the CO_2 and NH_4^+ bands we utilize are provided in Table 1. The band strength uncertainty for both the NH_3 and H_2O bands is 20% (M. Bouilloud et al. 2015).

4. Discussion

The exceptional quality of the MIRI MRS spectrum of the protostar ST6 in the LMC allowed us to identify five species of icy COMs: CH_3OH, CH_3CHO, CH_3CH_2OH, $HCOOCH_3$, and

CH_3COOH. Pre-JWST, CH_3OH was the most complex ice species detected and has been routinely observed toward Galactic protostars (e.g., A. C. A. Boogert et al. 2015 and references therein). In the LMC, CH_3OH ice was only weakly detected toward three protostars (IRAS 05328−6827, J. T. van Loon et al. 2005; ST6 and ST10, T. Shimonishi et al. 2016a). O. Nayak et al. (2024) presented a JWST MIRI MRS spectrum with prominent major simple ice and CH_3OH ice features for one protostar (Y3); however, no quantitative analysis was performed, and some band identifications are disputable (see Appendix H).

All the icy COMs larger than CH_3OH (four species) observed toward ST6 have been detected outside the Galaxy for the first time, while the detection of CH_3COOH ice constitutes the first conclusive detection of this icy COM in an astrophysical context. The detection of COMs in ices provides evidence that they are products of grain-surface chemistry and can form efficiently in a harsher environment than in the Galaxy.

4.1. Ice Column Density of CH_3OH

We determined the CH_3OH ice column density toward ST6 based on the 9.74 μm (1026 cm^{-1}) C–O stretching mode, detected with MIRI MRS with a high signal-to-noise ratio (see Figure E1). The resulting value of $N_{ice,\,CH_3OH}$ of $(2.8 \pm 0.2) \times 10^{17}\,cm^{-2}$ is about 23% lower than that reported for ST6 by T. Shimonishi et al. (2016a). The authors obtained $N_{ice,\,CH_3OH}$ of $(3.5 \pm 1.2) \times 10^{17}\,cm^{-2}$ using the 3.53 μm (2828 cm^{-1}) C–H stretching mode marginally detected with the ground-based ISAAC camera on the Very Large Telescope (VLT).

We utilized our NIRSpec IFU observations of ST6 to determine $N_{ice,\,CH_3OH}$ based on the same CH_3OH ice absorption band used by T. Shimonishi et al. (2016a; see Appendix D for details). We obtained $N_{ice,\,CH_3OH}$ of 3.56×10^{17} cm^{-2}, in excellent agreement with previous observations.

Differences in ice column densities based on different bands of the same species have been reported in the literature for Galactic protostars and dense clouds. For example, the differences of ∼20%–30% were reported for the low-mass protostar L1527 (K. Slavicinska et al. 2025b) and dense clouds (M. K. McClure et al. 2023) for the same CH_3OH bands utilized here. In another JWST study, N. G. C. Brunken et al. (2024) found a difference in the $^{12}CO_2$ column densities based on the 2.7 and 15.21 μm bands of ∼20%–25% toward two protostars and a factor of two toward one protostar. In addition, the authors found a factor of 1.6 difference in the ^{12}CO column densities based on the 2.35 and 4.67 μm bands for one protostar.

In addition to ice column density measurement errors (due to adopted continua and/or overlapping ice features, and band strength uncertainties), line-of-sight effects, which are due to radiative transfer effects (the effects of grain size, shape, and composition that change ice opacity), and chemical effects (different band strengths due to the ice morphology and density) may contribute to these differences.

4.2. Comparison to Galactic Protostars

In Figure 4, we compare simple and COM ice abundances with respect to H_2O ice measured toward ST6 with those of four Galactic protostellar objects with the JWST MIRI MRS detection of icy COMs larger than CH_3OH: NGC 1333 IRAS 2A (hereafter IRAS 2A; Y. Chen et al. 2024; W. R. M. Rocha et al. 2024b), B1–c (Y. Chen et al. 2024), IRAS 23385+6053 (hereafter IRAS 23385; W. R. M. Rocha et al. 2024b), and IRAS 18089−1732 (hereafter IRAS 18089; E. F. van Dishoeck et al. 2025).

IRAS 2A and B1–c are low-mass Class 0 protostars and well-studied hot corinos rich in gas-phase COMs (including $HOCH_2CHO$ for IRAS 2A; e.g., A. Coutens et al. 2015; V. Taquet et al. 2015; M. L. van Gelder et al. 2020). IRAS 2A is a protobinary system with two collimated jets, and B1–c is associated with a high-velocity outflow (e.g., J. K. Jørgensen et al. 2006).

IRAS 23385 is a massive protocluster in the main accretion phase (R. Cesaroni et al. 2019 and references therein; H. Beuther et al. 2023). Methanol and CH_3CN are the only COMs detected toward this source in the gas phase (C. Gieser et al. 2021). IRAS 18089 is a luminous massive protostellar object at the hot core stage, with millimeter/submillimeter spectra rich in gas-phase COMs (e.g., H. Beuther et al. 2004, 2005; S.-L. Qin et al. 2022). In terms of luminosity and evolutionary stage, ST6 is most similar to IRAS 23385.

The detection of CH_3CH_2OH, CH_3CHO, and $HCOOCH_3$ ices was reported toward all four Galactic protostars (see Figure 4). Additionally, CH_3OCH_3 ice was detected toward B1–c and IRAS 18089, and CH_3COOH ice was tentatively detected toward IRAS 2A. Y. Chen et al. (2024) claimed the detection of CH_3OCH_3 ice in the spectrum of B1–c; the suggestive detection of this species was also reported for IRAS 18089 by E. F. van Dishoeck et al. (2025).

Figure 4 demonstrates that in general, the fractional abundances of COM ices relative to H_2O ice measured toward ST6 are lower than those reported toward Galactic protostars (both low- and high-mass; see also Table 3). This trend was noted for CH_3OH by T. Shimonishi et al. (2016a), who only marginally detected the CH_3OH 3.53 μm ice absorption band toward 2 out of 11 LMC protostars in their sample. T. Shimonishi et al. (2016a) proposed the "warm ice chemistry" model to explain both the underabundance of solid CH_3OH and the observed overabundance of solid CO_2 in the LMC. When the dust temperature is high ($T \gtrsim 20$ K), e.g., due to a strong interstellar radiation field, as in the LMC, the hydrogenation of CO that leads to the formation of CH_3OH becomes less efficient due to the very rapid diffusion or evaporation of hydrogen atoms from grain surfaces. As a result of the much larger binding energy than hydrogen, CO remains on grain surfaces with increased mobility, enhancing the formation of CO_2. Methanol is a species directly linked to the production of larger COMs in both gas-phase and grain-surface chemistries, such as CH_3OCHO and CH_3OCH_3; thus, the less efficient CH_3OH formation leads to lower abundances of more complex species. The results of the recent modeling study by I. Jiménez-Serra et al. (2025) are consistent with the warm chemistry model proposed by T. Shimonishi et al. (2016a); the authors show that CH_3OH formation via CO hydrogenation is less efficient at $T > 12$ K across various state-of-the-art astrochemical codes.

For simple ices, we note the large difference in ice abundances between ST6 and Galactic protostars for H_2CO. Since H_2CO is mostly formed from the hydrogenation of CO on interstellar dust grains, warmer dust would lead to its underabundance. ST6's CH_4 ice abundance is also noticeably

lower than for Galactic protostars. The underabundance of CH_4 ice combined with the overabundance of CH_3COOH ice hints at a possibility that the higher UV radiation in the LMC photodissociates CH_4 more efficiently than in the Galaxy; the resulting CH_3 radical can recombine with the hydroxycarbonyl (HOCO) radical forming CH_3COOH (e.g., C. J. Bennett & R. I. Kaiser 2007).

In contrast to H_2CO and CH_4, the SO_2, HCOOH, $HCOO^-$, and OCN^- ice abundances compared to H_2O ice measured toward ST6 are similar to those observed toward the four Galactic protostars in Figure 4. This result indicates that ice abundances of these species likely do not (or only weakly) depend on the strength of the external UV radiation field.

HCOOH was included in R. T. Garrod et al.'s (2022) chemical modeling (see Section 4.4 for more details on models). The modeling results show that HCOOH ice abundance with respect to H_2O ice does not change after introducing the photodissociation-induced (PDI) reactions into the model; thus, the production of HCOOH ice is not expected to be enhanced in the LMC. Comparable $HCOO^-$ and OCN^- ice abundances between the LMC and the Galaxy are also not surprising, as salts are predominantly formed in thermally activated acid–base reactions (e.g., H. M. Cuppen et al. 2024 and references therein).

SO_2 ice observed toward protostars can be a product of hot gas chemistry followed by freeze-out or form in grain-surface reactions (S. B. Charnley 1997; T. Nguyen et al. 2024; R. Martín-Doménech et al. 2025). Since the gas-phase chemistry involves radicals such as SH and OH, the SO_2 gas-phase abundance depends on the strength of the local UV radiation field (e.g., M. L. van Gelder et al. 2021). Therefore, we would expect higher gas and ice abundances of SO_2 in the LMC. However, it was shown that a fraction of SO_2 in the ice mantles being the result of freeze-out of gaseous SO_2 can be quickly converted into other species by reactions with H atoms on the ice surface (T. Nguyen et al. 2024). SO_2 formed in ice from other S-bearing species through energetic processes can be incorporated in the bulk ice, where it is less likely to react with H atoms, and thus may remain detectable (e.g., C. N. Shingledecker et al. 2020). The solid SO_2 formation paths (and sulfur chemistry in general) are not well understood. Thus, is it not straightforward to predict the effects of the higher UV radiation fields in the LMC on the SO_2 ice abundance; our results indicate that they are not significant.

4.3. Comparison to Pre-JWST Results on Simple Ices

ST6 is one of a small sample of LMC protostars with ices previously studied with near-IR spectroscopy. The H_2O (3.05 μm), CO_2 (4.38 μm), and CO (4.67 μm) ice bands were first detected toward ST6 in the low spectral resolution AKARI spectroscopic data (2.5–5.0 μm): H_2O and CO_2 in T. Shimonishi et al. (2008; $R \sim 20$) and CO_2 and CO in T. Shimonishi et al. (2010; $R \sim 80$) at a spatial resolution of 5″–8″. The H_2O ice column density derived based on the AKARI data was hindered by large uncertainties. T. Shimonishi et al. (2016a) combined the AKARI data with the higher spectral ($R \sim 500$) and spatial (0.″6–0.″7) resolution VLT/ISAAC data (2.8–4.2 μm) and provided updated measurements for H_2O, CO_2, and CO ice column densities: $N_{H_2O,\ ice} = (62.10 \pm 8.62) \times 10^{17}$ cm^{-2}, $N_{CO_2,\ ice} = (21.5 \pm 6.2) \times 10^{17}$ cm^{-2}, and $N_{CO,\ ice} < 15 \times 10^{17}$ cm^{-2} (an upper limit due to the CO ice band being unresolved from either the CO gas absorption line or the XCN feature).

The H_2O and CO_2 ice column densities measured toward ST6 based on, respectively, the 13.2 and 15.2 μm bands covered by MIRI MRS are ∼85% (H_2O) and ∼15% (CO_2) higher than those measured with the combined AKARI and VLT/ISAAC data by T. Shimonishi et al. (2016a). The resulting CO_2/H_2O ratio of 21.5% is significantly lower than the previously reported value for ST6 of ∼35% and lies in the range observed toward Galactic protostars (11%–27% with a median of 19%; A. C. A. Boogert et al. 2015 and references therein). The new $N_{H_2O,\ ice}$ and $N_{CO_2,\ ice}$ determinations based on better-quality spectra for a larger sample of LMC YSOs may verify the CO_2/H_2O ratio in the LMC (the mean of 28.5% ± 11.6% based on 10 YSOs; T. Shimonishi et al. 2016a and references therein), potentially bringing it closer to the Galactic values. We note, however, that similarly to CH_3OH, there may be differences between $N_{H_2O,\ ice}$ and $N_{CO_2,\ ice}$ derived from different ice bands; thus, using the same bands for ice column determination toward all the sources in comparative studies would be optimal.

For the NH_3 ice, we obtained an abundance with respect to H_2O ice ($N_{NH_3,\ ice}/N_{H_2O,\ ice}$) toward ST6 of (3.35 ± 0.95)%. This result is consistent with the $N_{NH_3,\ ice}/N_{H_2O,\ ice}$ upper limit of <5% estimated by T. Shimonishi et al. (2016a) based on a possible detection of the NH_3 ice band at 9 μm (partially contaminated by PAH emission at 8.61 μm) in the Spitzer's Infrared Spectrograph spectrum (5–33 μm). Compared to Galactic YSOs, the $N_{NH_3,\ ice}/N_{H_2O,\ ice}$ ratio observed toward ST6 is not significantly different; $N_{NH_3,\ ice}/N_{H_2O,\ ice}$ is about ∼7% for Galactic high-mass and 3%–10% for low-mass YSOs (e.g., A. C. A. Boogert et al. 2015). Interestingly, gas-phase NH_3 has only been detected toward one star-forming region in the LMC, namely, N159W, with a fractional abundance relative to H_2 of $\sim 4 \times 10^{-10}$, 1.5–2 orders of magnitude lower than typical values observed in Galactic star-forming regions even after correcting for the metallicity difference and beam dilution effects (J. Ott et al. 2010).

4.4. $C_2H_4O_2$ Structural Isomers

Methyl formate ($HCOOCH_3$) and acetic acid (CH_3COOH) are structural isomers. We compare the $CH_3COOH/HCOOCH_3$ ice column density ratio observed toward ST6 to those predicted in R. T. Garrod et al. (2022) using the astrochemical gas-grain code MAGICKAL, a state-of-the-art three-phase model optimized for simulating the chemistry in cold dense cores and hot cores. MAGICKAL solves a set of rate equations describing chemical kinetics not only in the gas but also on grain surfaces and within ice mantles, where COMs are believed to form.

For the final model that includes all the processes considered in their analysis, R. T. Garrod et al. (2022) provide solid-phase fractional abundances with respect to total hydrogen of $(5.67, 112) \times 10^{-9}$ for (CH_3COOH, $HCOOCH_3$), resulting in a $CH_3COOH/HCOOCH_3$ ice ratio of 0.051. The observed $CH_3COOH/HCOOCH_3$ ratio of ∼2.4 is a factor of ∼46 times higher than predicted. We note, however, that ST6's $CH_3COOH/HCOOCH_3$ ice ratio is only a factor of 4 higher than that of the first model in R. T. Garrod et al.'s (2022) set of models with increasing complexity that includes PDI reactions and a factor of ∼6 higher than predicted by the subsequent model, "PDI2." In the PDI2 implementation,

photodissociation products in the ice mantles (excluding hydrogen) are allowed to recombine immediately to reform the original molecules if they do not find a reaction partner.

The R. T. Garrod et al. (2022) model results demonstrate that CH_3COOH shows a different chemical behavior from $HCOOCH_3$, its structural isomer. One of the characteristics of CH_3COOH differentiating it from $HCOOCH_3$ is its very early production (dominating its total production) that is strongly associated with photoprocessing of simple ices by external UV photons (via PDI nondiffusive reactions). Therefore, the high ice abundance of CH_3COOH observed in the LMC could be attributed to the higher UV flux in the LMC's environment compared to the Galaxy (not considered in R. T. Garrod et al.'s 2022 Galactic models). Alternatively, another species with no laboratory data currently available may also contribute to ST6's spectrum in the 7.6–8.0 μm wavelength range, reducing the amount of CH_3COOH required to obtain the best fit to the observations.

The MAGICKAL model grid for a selection of key parameters appropriate for the LMC (such as elemental abundances, cosmic-ray ionization rate, and UV field strength) is under development (M. Jin & R. Garrod 2025, private communication). These models will allow us to better understand both the solid and gas-phase molecular abundances observed toward the LMC sources.

4.5. Exploring Potential Assignments to Unidentified Ice Bands

The high-quality MIRI MRS spectrum of ST6 shows many ice bands with no prior chemical assignments, e.g., at about 5.72, 5.78, 5.84, 5.89, 7.28, 7.34, 7.75, 7.85, 8.12, 8.80, 8.88, 9.03, 9.23, and 9.34 μm (see Figure G3).

As the isomer of two ice species conclusively detected toward ST6 (CH_3COOH and $HCOOCH_3$), glycolaldehyde ($HOCH_2CHO$) is a good candidate for the species responsible for some of the unidentified ice bands in the spectrum of ST6. The presence of the $HOCH_2CHO$ ice would be particularly interesting since it is a precursor of ribose, which is a major constituent of ribonucleic acid (e.g., C. Meinert et al. 2016) and was the first sugar-related molecule detected in interstellar space in the gas phase (e.g., J. M. Hollis et al. 2000).

The comparison between the $HOCH_2CHO$:CO and $HOCH_2CHO$:CO_2 laboratory spectra and ST6's residual spectrum after subtracting the contribution from known species reveals a good match of the latter to the isolated ice band at 5.72 μm. It also shows that $HOCH_2CHO$ can contribute to the features at 5.84, 7.75, 7.85, 8.12, and 9.03 μm (see Appendix G for details). The only discrepancy is observed for the $\sim$7.3 μm band. However, this mismatch is not enough to completely rule out the presence of $HOCH_2CHO$ at this stage since the shape of this specific feature is highly dependent on the chemical mixture (see Figure G3). No experimental infrared spectra for $HOCH_2CHO$ in other astrophysically relevant ice mixtures are currently available, making it impossible for us to conduct additional verification of the presence of $HOCH_2CHO$ in ST6's spectrum using the laboratory data. As the result, the detection of $HOCH_2CHO$ toward ST6 is inconclusive.

We perform an additional test based on the comparison between the data and R. T. Garrod et al.'s (2022) chemical model predictions. Under the assumption that the isolated 5.72 μm ice band is the C=O stretching mode of $HOCH_2CHO$ and that $HOCH_2CHO$ is the only contributing species, we determine the $HOCH_2CHO$ ice column density of $(0.09 \pm 0.04) \times 10^{17}$ cm^{-2} using the local continuum method (see Appendix G for details).

We compare the $HCOOCH_3/HOCH_2CHO$ and $CH_3COOH/HOCH_2CHO$ ice column density ratios observed toward ST6 to those predicted in R. T. Garrod et al. (2022; Section 4.4). For $HOCH_2CHO$, the authors provide a solid-phase fractional abundance with respect to total hydrogen of 8.33×10^{-8} for their final model, resulting in the $HCOOCH_3/HOCH_2CHO$ and $CH_3COOH/HOCH_2CHO$ ratios of 1.3 and 0.07, respectively.

ST6's $HCOOCH_3/HOCH_2CHO$ ice ratio of 1.2 is in very good agreement with the R. T. Garrod et al. (2022) model prediction (and thus supports the identification of $HOCH_2CHO$ toward ST6); however, the $CH_3COOH/HOCH_2CHO$ ice ratio of 2.9 is $\sim$42 times higher than predicted. The latter ratio is very similar to the $CH_3COOH/HCOOCH_3$ ice ratio, which is expected, as $HCOOCH_3$ and $HOCH_2CHO$ show a similar chemical behavior, distinct from CH_3COOH. Similarly to the $CH_3COOH/HCOOCH_3$ ice ratio discussed in Section 4.4, a much better agreement with the observations is found for the PDI and PDI2 models that predict $CH_3COOH/HOCH_2CHO$ ice ratios of 1.8 and 2.9, respectively.

We highlight that we could not find a carrier for the features at 5.78, 5.89, 7.28, 7.34, 8.80, 8.88, 9.23, and 9.34 μm or other contributing species to the features associated with $HOCH_2CHO$. It is interesting to note that an absorption excess at 9.03 μm that can be partially attributed to $HOCH_2CHO$ is also seen toward the protostar Ced 110 IRS4A (strongly overlapping with H_2O gas-phase lines) and reported as an unidentified feature (W. R. M. Rocha et al. 2025). No investigation for the presence of $HOCH_2CHO$ toward Ced 110 IRS4A has been performed.

5. Conclusions

Based on the analysis of the JWST MIRI MRS spectrum of the protostar ST6, we confirm the presence of COMs in interstellar ices in the low-metallicity and high UV flux environment of the LMC. The high quality of the spectrum allows us to identify four COM ices more complex than CH_3OH: CH_3CHO, CH_3CH_2OH, $HCOOCH_3$, and CH_3COOH. The detection of COMs in ices provides evidence that they are products of grain-surface chemistry. We quantified the large COM and simple (except H_2O and CO_2) ice abundances with respect to H_2O ice for the first time in the LMC and found differences when compared to those measured toward Galactic protostars; these differences may be the result of the lower metallicity and higher UV flux in the LMC.

Our conclusions are based on a single LMC and only four Galactic sources; a larger sample of protostars with measured simple and COM ice abundances in both galaxies is needed to confirm our results. Local measurements of both metallicity and UV radiation field strength in the LMC would also be valuable for the interpretation of the observations.

The ENIIGMA best fit to the MIRI MRS spectrum of ST6 shows that there is room for contributions from other species. Unidentified ice bands are present in and outside the ENIIGMA fitting range. We have found evidence that several of these features could be attributed to $HOCH_2CHO$, a precursor of biomolecules; however, the lack of the laboratory infrared spectra of $HOCH_2CHO$ ice astronomically relevant

mixtures prevented us from resolving the discrepancy between the data and the existing (likely contaminated) $HOCH_2CHO$:CO and $HOCH_2CHO$:CO_2 models. As a result, the presence of $HOCH_2CHO$ toward ST6 remains inconclusive. More experimental data for COM ices are needed to more accurately reproduce the observed mid-IR spectra of protostars.

The low-metallicity environment of the LMC is similar to galaxies at earlier cosmological epochs ($z \sim 1$–1.5; e.g., Y. C. Pei et al. 1999; D. Mehlert et al. 2002; P. Madau & M. Dickinson 2014); thus, our results give us a glimpse into the chemical complexity in star-forming regions in the earlier epochs of the Universe.

Acknowledgments

We thank the anonymous referee for insightful comments that helped us improve the manuscript. This work is based on observations made with the NASA/ESA/CSA James Webb Space Telescope. The data were obtained from the Mikulski Archive for Space Telescopes at the Space Telescope Science Institute (STScI), which is operated by the Association of Universities for Research in Astronomy, Incorporated, under NASA contract NAS5-03127 for JWST. These observations are associated with program #3702. The uncalibrated data for ST6 were obtained from MAST and processed as described in Section 2. The archival versions of the MIRI MRS and NIRSpec IFU data cubes for ST6 (not used in the analysis presented in this Letter) can be accessed via DOI: 10.17909/0t1j-zw13. Support for program #3702 was provided through a grant from the STScI (JWST-GO-03702.014-A) under NASA contract NAS5-03127. The material is based upon work supported by NASA under award number 80GSFC24M0006 (M.S.). R.H.G. acknowledges support from the Deutsche Forschungsgemeinschaft (DFG, German Research Foundation) through project SCHI 561/1-1 and the Collaborative Research Center 1601 (SFB 1601, sub-project A1), funded by the DFG – project ID 500700252. MIRI development was an equal collaboration between European and US partners. The MIRI optical system was built by a consortium of European partners from Belgium, Denmark, France, Germany, Ireland, the Netherlands, Spain, Sweden, Switzerland, and the United Kingdom. They were led by Gillian Wright, the European Principal Investigator, and Alistair Glasse, Instrument Scientist. EADS-Astrium (now Airbus Defense and Space) provided the project office and management. The full instrument test was conducted at Rutherford Appleton Laboratory. The Jet Propulsion Laboratory (JPL) provided the core instrument flight software and the detector system, including infrared detector arrays obtained from Raytheon Vision Systems; collaborated with Northrop Grumman Aerospace Systems on the cooler development and test; and managed the US effort. The JPL Instrument Scientist is Michael Ressler, and the MIRI Science Team Lead is George Rieke. NIRSpec was built for the European Space Agency by Airbus Industries; the microshutter assembly and detector subsystems were provided by NASA. Dr. Peter Jakobsen guided NIRSpec's development until his retirement in 2011. Dr. Pierre Ferruit is the current NIRSpec PI and ESA JWST project scientist. This research made use of APLpy, an open-source plotting package for Python (T. Robitaille & E. Bressert 2012).

Facilities: JWST, MAST.

Appendix A
The Location of ST6 in the LMC and Its Local Environment

ST6 (e.g., T. Shimonishi et al. 2008, 2010, 2016a; 053941.12−692916.8, R. A. Gruendl & Y. Chu 2009, L. R. Carlson et al. 2012, O. C. Jones et al. 2017; HSOBMHERICC J84.921913−69.48777, J. P. Seale et al. 2014) is a deeply embedded massive protostar in the star-forming region LHA 120–N158 in the LMC (hereafter N158, K. G. Henize 1956; $L = (6.6 \pm 2.5) \times 10^3\ L_{\odot}$, T. Shimonishi et al. 2010), $\sim 25''$ south of 30 Doradus (see Figure 1). The position of N158/ST6 is indicated in the Herschel far-IR three-color mosaic of the LMC in the left panel of Figure 1. Figure 1 also shows the mid-IR (Spitzer) and optical (Hα) view of the star-forming region N158. The optical nebula N158 consists of two distinct regions: the Hα-bright region in the southwest (N158 C) excited by the OB association LH 101 (P. B. Lucke & P. W. Hodge 1970) and the Hα superbubble in the northeast hosting the OB association LH 104 and coinciding with diffuse soft X-ray emission (M. Sasaki et al. 2011). N158C is the site of the most vigorous star formation in the region, as indicated by the presence of bright mid-to-far-IR (M. Meixner et al. 2006, 2013) and CO (T. Wong et al. 2011; K. Grishunin et al. 2024) emission, and the highest concentration of massive YSOs in N158 (R. A. Gruendl & Y. Chu 2009; L. R. Carlson et al. 2012). ST6 is associated with an isolated CO molecular cloud, $\sim 2.'6$ northeast of N158C and its associated giant molecular cloud and $\sim 3.'2$ south of the rim of the superbubble. In the inset image in the right panel of Figure 1, we show a zoom-in on ST6 and its immediate surroundings with the ^{13}CO (2–1) contours overlaid; these are the highest-resolution molecular gas observations of N158 obtained with the Atacama Compact Array (the synthesized beam size of $7'' \times 7''$; A. Bolatto & E. Tarantino 2025, private communication). The velocity of the molecular cloud associated with ST6 ($\sim$224 km s^{-1}) is $\sim$30 km s^{-1} lower than the velocity of the bulk of the molecular gas in N158 ($\sim$256 km s^{-1}) and more consistent with the CO gas extending to the south toward the star-forming region N160.

Appendix B
Supplementary Material on the Spectral Extraction and Initial Analysis

In this Appendix, we include figures providing additional information on the MIRI MRS spectral extraction (Figure B1) and the subsequent analysis, including the global continuum and silicate subtraction (Figure B2). We also illustrate the local continuum subtraction preceding the ENIIGMA fitting described in Section 3.2 (Figure B3). Finally, Figure B4 displays the guiding points around the 7−10 μm range and the H_2O and NH_4^+ ice absorption profiles overlaid on the silicate-subtracted spectrum of ST6 (the same as in Figure B3). This comparison validates the position of the guiding points that are used to trace the local continuum around the icy COMs region. Due to intrinsic uncertainties in the ice models and the continuum itself, the guiding points may slightly deviate from the H_2O and NH_4^+ models.

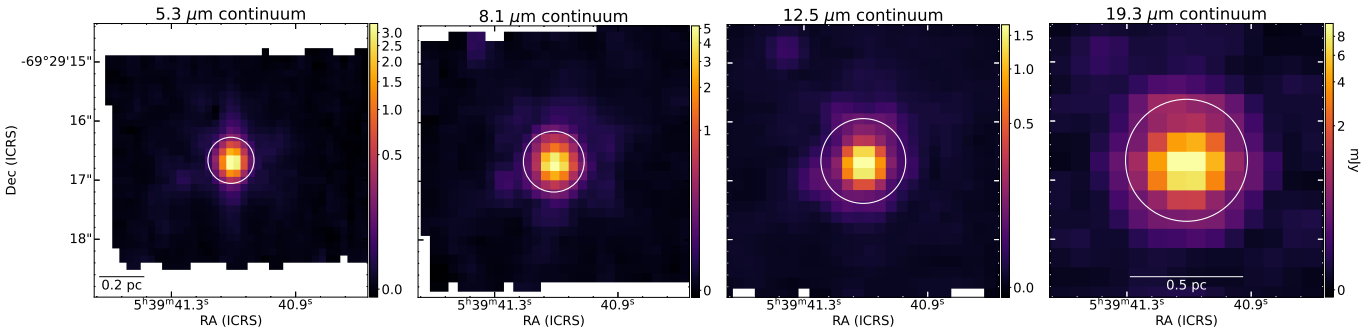


Figure B1. The MIRI MRS channel maps corresponding to the continuum emission detected toward ST6 at (from left to right) 5.3, 8.1, 12.5, and 19.3 μm. Overlaid on each image is the circular spectral extraction aperture with a diameter of 3 $\times$ $\mathrm{FWHM_{PSF,\lambda}}$, where $\mathrm{FWHM_{PSF,\lambda}}$ is the empirically derived FWHM of the MIRI MRS PSF at a given wavelength (λ; see Section 2 for details).

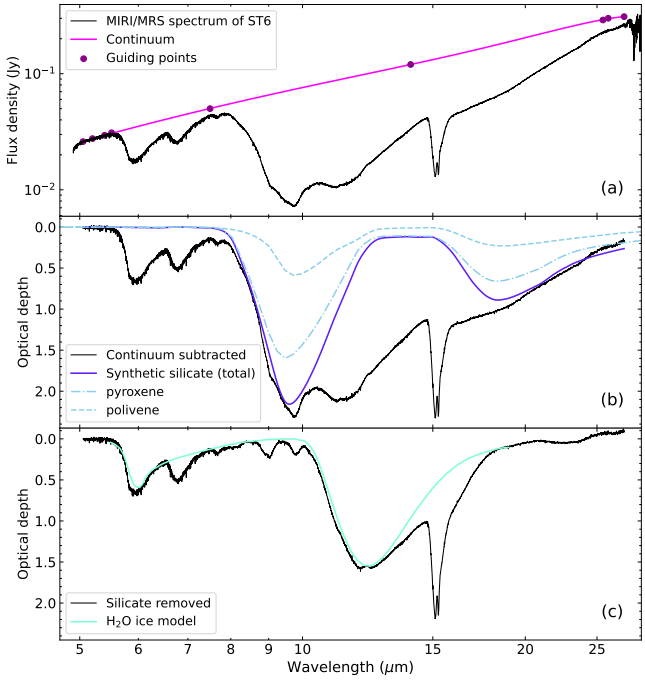


Figure B2. The top and middle panels demonstrate, respectively, the global continuum and silicate subtraction procedure applied to the MIRI MRS spectrum of ST6. The continuum was determined by fitting a fourth-order polynomial function (shown in magenta in the top panel) to selected guiding points (indicated in purple). The silicate profile shown in blue in the middle panel is a combination of two laboratory silicate spectra (pyroxene and polivene, plotted individually in light blue). Bottom panel: the spectrum of ST6 after the global continuum and silicate subtraction, with the H_2O ice model overlaid in aquamarine.

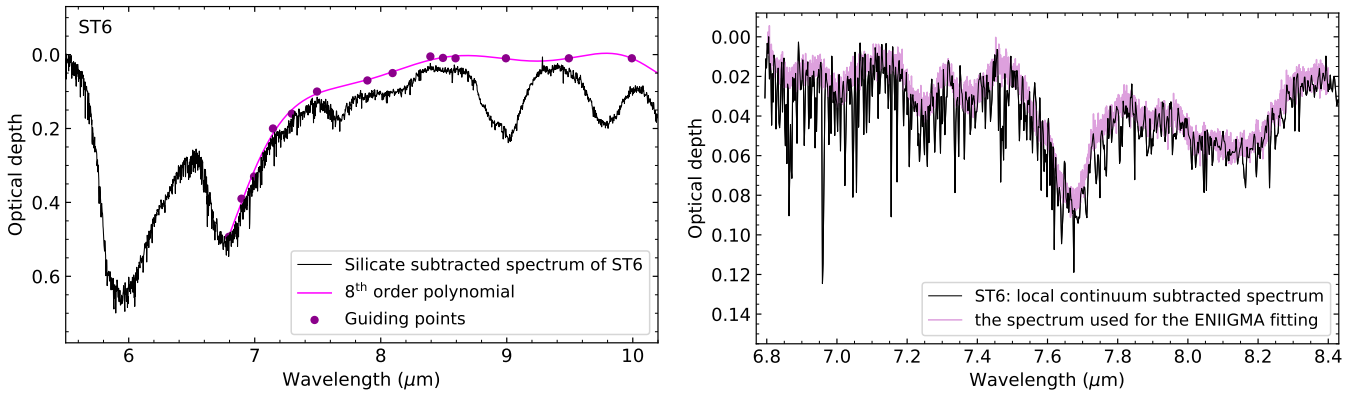


Figure B3. The magenta curve in the left panel is a eighth-order polynomial function fit through the guiding points (indicated with purple dots), tracing the local continuum around the "COMs region." The local-continuum-subtracted spectrum between 6.8 and 8.4 μm (corresponding to the "COMs region") is shown in the right panel (black). Multiple absorption lines resembling noise are H_2O gas-phase absorption lines. The underlying spectrum plotted in light violet was used for the ENIIGMA fitting (see Section 3.2 for details).

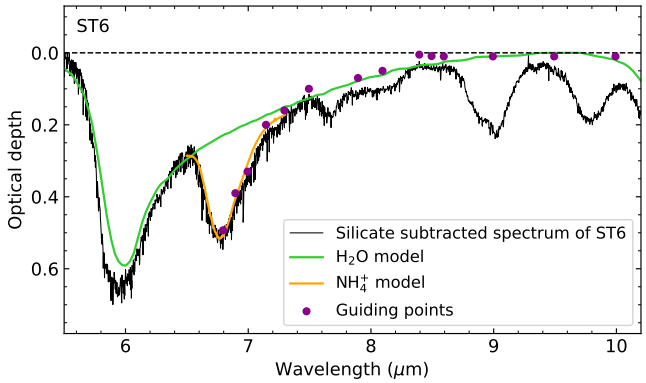


Figure B4. The silicate-subtracted spectrum of ST6 and the local continuum guiding points (the same as in Figure B3) are compared to H_2O (green; Figure B2) and NH_4^+ (orange; Figure E2) models to a posteriori verify the selection of guiding points.

Appendix C
The ENIIGMA Fitting: The Preparation of the Spectrum and Laboratory Data Used

Prior to the spectral fitting with ENIIGMA, we removed the gas-phase features mostly due to H_2O vapor by using a spline function between 5.5 and 8.6 μm to account only for the absorption bands due to ices. To guide the spline function, anchor points were used across the spectral range. This step allows ENIIGMA to fit only the ice features and not be affected by the relatively strong gas absorption lines. The noise (see Section 2) is accounted for during the ENIIGMA fit.

In Table 2, we provide detailed information on all the laboratory ice spectra used in the ENIIGMA fitting described in Section 3.2.

In Figure C1, we present individual components of the ENIIGMA fit to the MIRI MRS spectrum of ST6 shown in Figure 3.

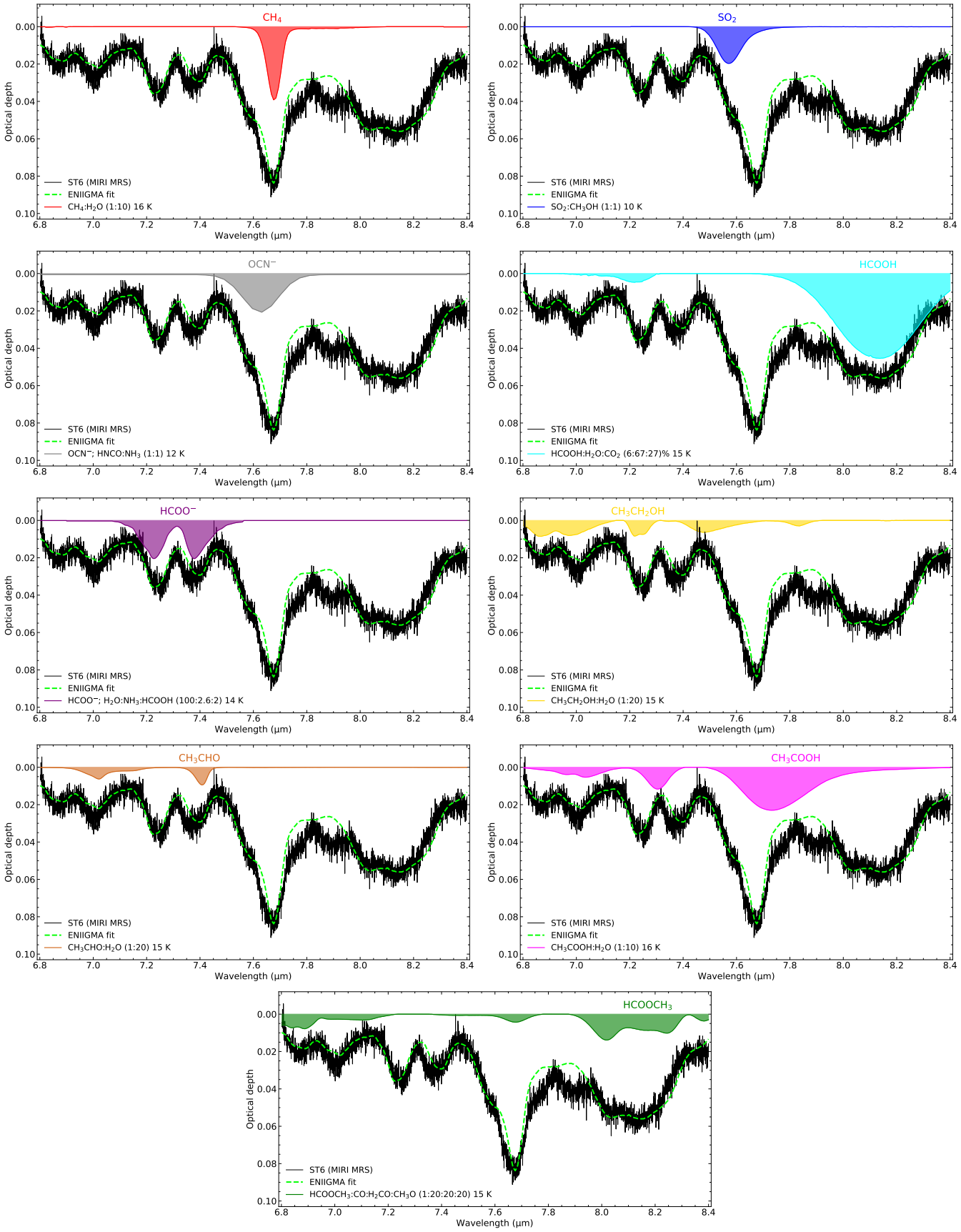


Figure C1. Individual components of the ENIIGMA fit to the MIRI MRS spectrum of ST6 in the 6.8–8.4 μm wavelength range, color-coded as in Figure 3. The combined ENIIGMA fit is shown as a dashed green line in each panel. For each component, the legend provides information on the ice mixture and temperature used to obtain the laboratory spectrum.

Table 2
Laboratory Data Used in the ENIIGMA Fitting

Mixture[a]	Temperature (K)	Database	References
CH_4:H_2O (1:10)	16	LIDA	W. R. M. Rocha et al. (2017)
OCN^-:HNCO:NH3 (1:1)[b]	12	LIDA	J. H. Novozamsky et al. (2001)
$HCOO^-$:H_2O:NH_3:HCOOH (100:2.6:2)[b]	14	LIDA	O. Gálvez et al. (2010)
HCOOH:H_2O:CO_2 (6:68:26%)	15	LIDA	S. E. Bisschop et al. (2007)
SO_2:CH_3OH (1:1)	10	LIDA	A. C. A. Boogert et al. (1997)
CH_3CHO:H_2O (1:20)	15	LIDA	J. Terwisscha van Scheltinga et al. (2018)
CH_3CH_2OH:H_2O (1:20)	15	LIDA	J. Terwisscha van Scheltinga et al. (2018)
$HCOOCH_3$:CO:H_2CO:CH_3OH (1:20:20:20)	15	LIDA	J. Terwisscha van Scheltinga et al. (2021)
CH_3COOH:H_2O (1:10)	16	NASA	R. L. Hudson & P. A. Gerakines (2019)

Notes.
[a] The format is a species of interest followed by a matrix.
[b] Only in the case of the ions, the ratios of the mixtures correspond to the deposition values. The ratios of the products are not available.

Appendix D
Determination of the OCN^- and CH_3OH Ice Column Density Based on the NIRSpec IFU Data

We take advantage of the availability of the NIRSpec IFU spectrum of ST6 in our program to constrain the cyanate anion (OCN^-) ice column density for the ENIIGMA fitting. We also use the NIRSpec IFU spectrum to determine the CH_3OH ice column density to compare to that based on the MIRI MRS spectrum.

For the NIRSpec IFU observations, we used the G395H/F290LP disperser/filter combination covering a wavelength range of 2.87–5.27 μm, with a nominal resolving power of $\sim$2700. The data were background-subtracted, and the warm pixel and leakcal (to mitigate the effects of leakage through the microshutter assembly) corrections were applied. Similarly to MIRI MRS, we use the wavelength-dependent aperture size to extract the NIRSpec IFU spectra; the diameter of the aperture is $3 \times \mathrm{FWHM}_{\mathrm{PSF},\lambda}$. A detailed description of the NIRSpec IFU data reduction and analysis will be provided in a future publication.

To determine the OCN^- ice column density, we utilized the C≡N stretching band of OCN^- at 4.62 μm (2164.5 cm^{-1}). Based on the observations of Galactic protostars, F. A. van Broekhuizen et al. (2005) found that the "XCN" absorption feature at 4.62 μm (2164.5 cm^{-1}) can be described by a combination of two Gaussian components centered at 2165.7 cm^{-1} ($\sim$4.62 μm; FWHM = 26 cm^{-1}) and 2175.4 cm^{-1} ($\sim$4.60 μm; FWHM = 15 cm^{-1}). Only the 2165.7 cm^{-1} component can be attributed to OCN^- ice, and for many protostars, the contribution from the second component has to be removed for the OCN^- ice column density calculations. For ST6, a single Gaussian component at 2165.7 cm^{-1} (OCN^- ice) with an amplitude (the peak optical depth) of 0.065 describes the data well (see Figure D1). We use the integrated area under the Gauss function and the band strength of 1.3×10^{-16} cm $\mathrm{molecule}^{-1}$ (F. A. van Broekhuizen et al. 2005) to determine the OCN^- ice column density from Equation (3).

We also utilize our NIRSpec IFU observations of ST6 to determine the CH_3OH column density based on the 3.53 μm (2828 cm^{-1}) C–H stretching mode and the local continuum method. The contribution from the partially overlapping $\sim$3.47 μm absorption band was accounted for as described in M. K. McClure et al. (2023); see also Figure D2. The 3.47 μm band has been attributed to ammonia hydrate ($NH_3 \cdot H_2O$; E. Dartois & L. d'Hendecourt 2001); however, its carrier is still uncertain (see, e.g., T. Shimonishi et al. 2016a). We adopted the band strength of 5.19×10^{-18} cm $\mathrm{molecule}^{-1}$ (with an uncertainty of 5%) for the CH_3OH 3.53 μm band (R. L. Hudson et al. 2024). We discuss differences in CH_3OH ice column densities based on different bands in Section 4.

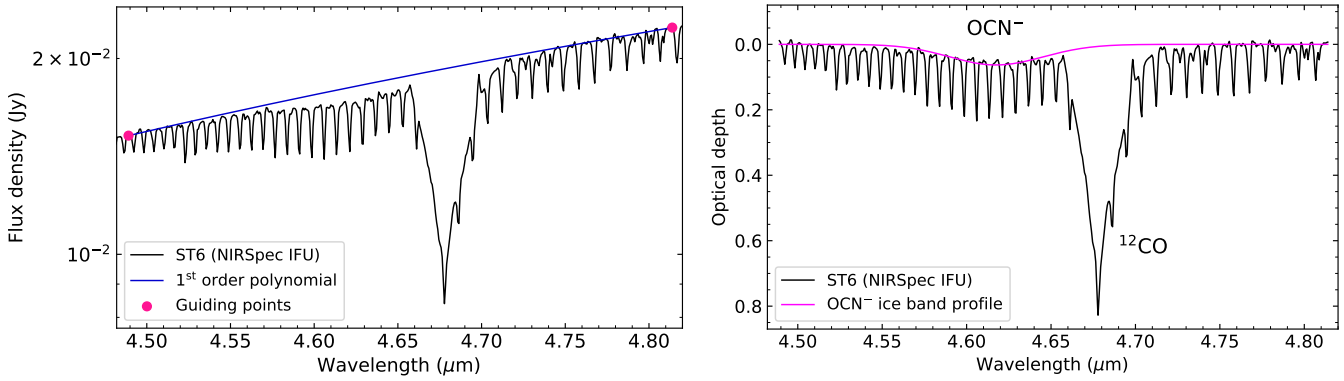


Figure D1. The NIRSpec IFU spectrum of ST6 covering the C≡N stretching mode of OCN^- ice at 4.59 μm and the CO stretching mode of ^{12}CO ice at 4.67 μm. The narrow absorption lines are from the *R* (4.3–4.7 μm) and *P* (4.7–5.2 μm) branches of the CO rovibrational transitions. The local-continuum-subtracted procedure is presented in the left panel. A first-order polynomial function was fit to the indicated guiding points to determine the local continuum. The local-continuum-subtracted spectrum is shown in the right panel. The OCN^- ice band is described by a single Gaussian component.

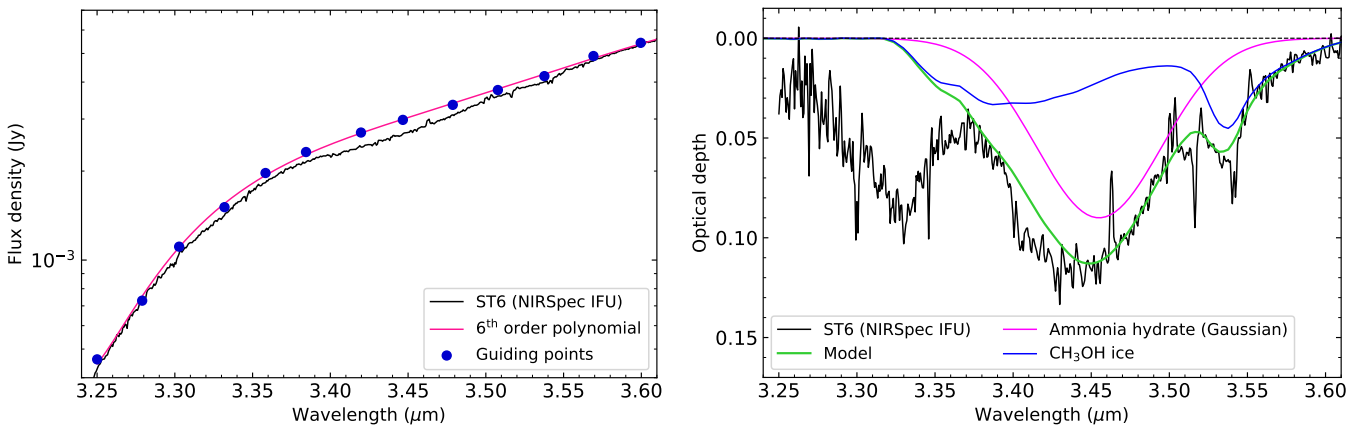


Figure D2. The NIRSpec IFU 3.25–3.60 μm spectrum of ST6 covering the C–H stretching mode of CH_3OH ice at 3.53 μm. The left panel illustrates the local continuum subtraction procedure. A sixth-order polynomial function was fit to the guiding points indicated in the plot. The local-continuum-subtracted spectrum is shown in the right panel. The 3.47 μm feature attributed to ammonia hydrate overlapping with CH_3OH ice at 3.53 μm is represented by a simple Gaussian function (shown in magenta). The laboratory spectrum of CH_3OH at 10 K is shown in blue (D. M. Hudgins et al. 1993), and the combined (CH_3OH and $NH_3{\cdot}H_2O$) spectrum is shown in green.

Appendix E
Local Continuum Subtraction for the NH_3, CH_3OH, CO_2, and NH_4^+ Ice Bands

We illustrate the local continuum subtraction procedure for the spectral range covering the NH_3 (9.0 μm) and CH_3OH (9.74 μm) ice bands and the CO_2 (15.27 μm) ice band in Figure E1 and the NH_4^+ (6.8 μm) ice band in Figure E2. The description of the subsequent ice column density determination is provided in Sections 3.4.1 and 3.4.2 for COM and simple ices, respectively.

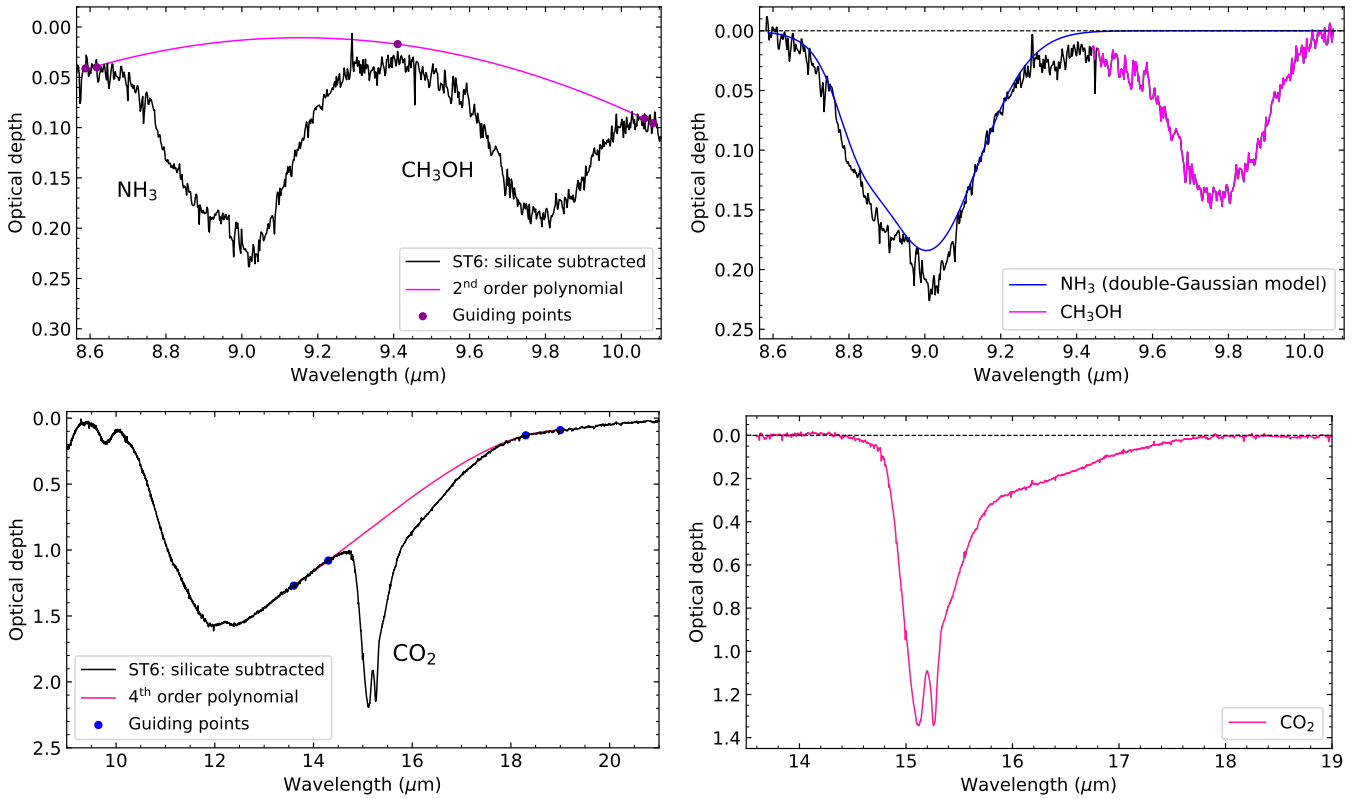


Figure E1. The left panel shows the local continuum subtraction procedure for the wavelength range covering NH_3 and CH_3OH (top) and CO_2 (bottom) ice absorption bands. A second- (top left) or fourth- (bottom left) order polynomial function was fit to the guiding points indicated in the plots. The right panel shows the corresponding local-continuum-subtracted spectra. The double-peaked Gaussian function shown in the upper right panel was used to determine the NH_3 ice column density toward ST6 (see Section 3.4 for details).

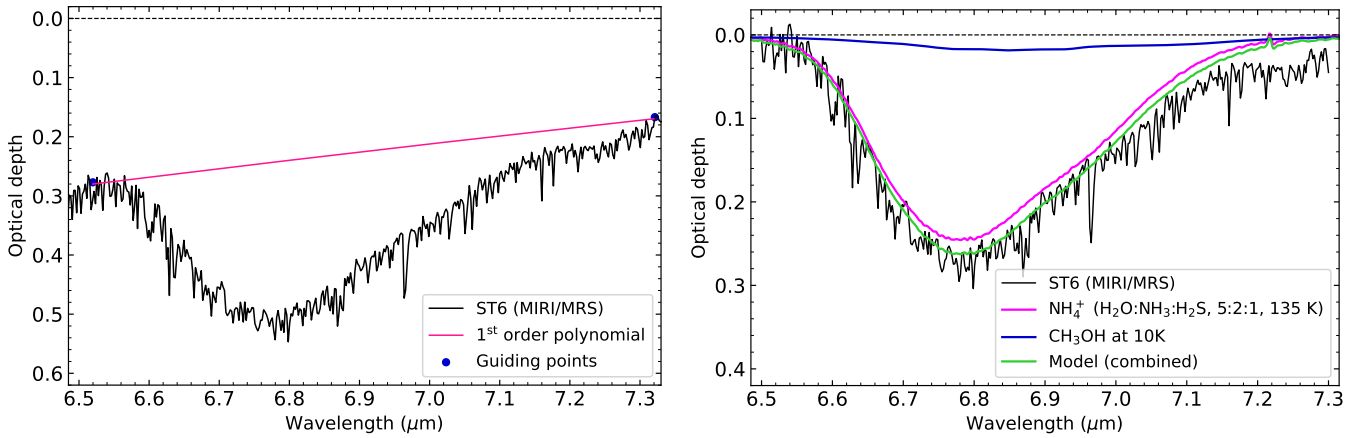


Figure E2. In the left panel, we show the local continuum subtraction procedure for the 6.8 μm ice feature attributed to the ammonium (NH_4^+) bend with the contribution from the CH_3OH C–H reformation mode. A first-order polynomial function was fit to the guiding points indicated in the plot and represents the local continuum. The local-continuum-subtracted spectrum is shown in the right panel. The contribution from the CH_3OH C–H reformation mode to the 6.8 μm ice band was estimated by matching the CH_3OH laboratory spectrum (shown in blue; D. M. Hudgins et al. 1993) to the intensity of the CH_3OH ice band at 9.74 μm. The contribution from NH_4^+ is shown in magenta (K. Slavicinska et al. 2025a), and the combined spectrum is shown in green.

Appendix F
Molecular Ice Abundance with Respect to Water Ice Ratios between ST6 and Galactic Protostars

In Table 3, we provide supplementary information to Figure 4, namely, the ice abundance with respect to H_2O ice ratios between ST6 and Galactic protostars with the COM ice detections. This information allows for a more detailed view of differences in ice abundances measured toward ST6 and Galactic protostars revealed by the bar plot in Figure 4.

Table 3
Ice Abundances with Respect to Water Ice (X_{ice}): Ratios between ST6 and Galactic Protostars[a]

Species	$X_{ice}(ST6)/X_{ice}(YSO_{Gal})$			
	IRAS 18089 (HM)	IRAS 23385 (HM)	IRAS 2A[b] (LM)	B1–c (LM)
CH_4	$0.25^{+0.11}_{-0.10}$	$0.14^{+0.07}_{-0.05}$	$0.28^{+0.17}_{-0.12}$	$0.12^{+0.08}_{-0.07}$
SO_2	$0.94^{+0.45}_{-0.46}$	$0.78^{+1.97}_{-0.82}$	$0.50^{+1.00}_{-0.21}$	>0.52
HCOOH	$0.72^{+0.31}_{-0.35}$	$0.65^{+0.39}_{-0.32}$	$0.74^{+0.60}_{-0.41}$	$1.68^{+1.05}_{-1.11}$
H_2CO	$0.02^{+0.01}_{-0.01}$	>0.015	$0.05^{+0.04}_{-0.03}$	$0.12^{+0.07}_{-0.06}$
$HCOO^-$	$0.60^{+0.38}_{-0.42}$	$1.23^{+1.08}_{-1.13}$	$0.50^{+0.44}_{-0.46}$	$0.63^{+0.49}_{-0.52}$
OCN^-	$0.41^{+0.19}_{-0.18}$	$1.34^{+1.28}_{-0.62}$	$0.62^{+0.51}_{-0.16}$	$0.48^{+0.30}_{-0.29}$
CH_3OH	$0.14^{+0.06}_{-0.06}$	>0.07	$0.39^{+0.12}_{-0.12}$	$0.21^{+0.08}_{-0.08}$
CH_3CH_2OH	$0.29^{+0.15}_{-0.15}$	$0.23^{+0.14}_{-0.13}$	$0.35^{+0.15}_{-0.33}$	$0.51^{+0.34}_{-0.34}$
CH_3CHO	$0.35^{+0.20}_{-0.19}$	$0.53^{+0.40}_{-0.33}$	$0.32^{+0.16}_{-0.17}$	$0.32^{+0.22}_{-0.22}$
$HCOOCH_3$	$0.30^{+0.17}_{-0.15}$	$0.14^{+0.07}_{-0.06}$	$1.44^{+1.57}_{-0.88}$	$0.50^{+0.37}_{-0.34}$
CH_3COOH	>0.33	⋯	$0.77^{+0.40}_{-0.31}$	>2.88

Notes.
[a] IRAS 18089 and IRAS 23385 are high-mass (HM), while IRAS 2A and B1–c are low-mass (LM) protostars.
[b] For IRAS 2A, H_2CO and CH_3COOH detections are tentative.

Appendix G
Exploring Potential Assignments to Unidentified Ice Bands: Glycolaldehyde

G.1. Laboratory Infrared Spectra of $HOCH_2CHO$

The laboratory infrared spectra of $HOCH_2CHO$ were obtained as part of a master's thesis project at Leiden University. The experiment was performed in 2021 by Casper F. Spijker under the supervision of Dr. Marina Gomes Rachid. Since this work has not been described in the literature, we provide a summary of the experimental procedure used to measure the $HOCH_2CHO$ spectra. These measurements were performed using the Infrared Absorption Setup for Ice Spectroscopy at the Leiden Laboratory for Astrophysics. The pressure inside the experimental chamber was 2×10^{-9} mbar, and a germanium substrate was used for the vapor deposition. The infrared spectra of the ice were measured with a Fourier-transform infrared spectrometer covering a wavenumber range between 4000 and 400 cm^{-1} (2.5−25 μm) and a resolution of 1 cm^{-1}.

In this Letter, we use the following ice mixtures: $HOCH_2CHO$:CO (1:20) and $HOCH_2CHO$:CO_2 (1:20) at 15 K. Individual lines are used to deposit the vapor inside the chamber. A gas bottle of CO or CO_2 is connected to the chamber via the deposition lines. In the case of $HOCH_2CHO$, the glycolaldehyde powder is placed in a test tube and immersed in a water bath at 373 K, which is connected to the chamber via a separate deposition line.

The laboratory infrared spectra of $HOCH_2CHO$:CO (1:20) and $HOCH_2CHO$:CO_2 (1:20) at 15 K are shown in Figure G1; they are available in the LIDA database.

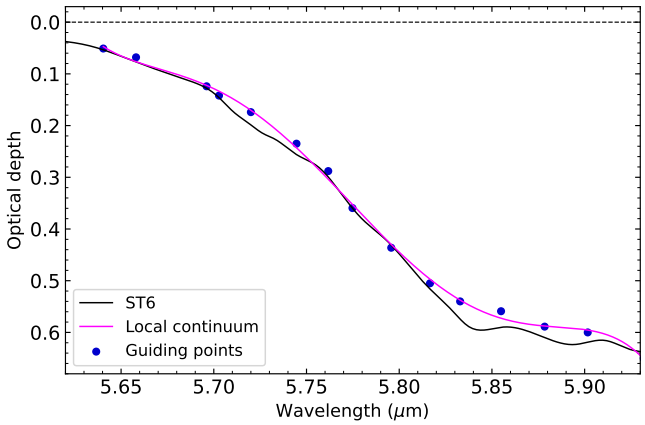


Figure G2. The local continuum subtraction procedure for the ice bands at 5.72, 5.78, and 5.84 μm. An eighth-order polynomial function was fit to the guiding points indicated in the plot. The local-continuum-subtracted spectrum is shown in the upper panel of Figure G3. The 5.72 μm band is utilized to determine $N_{ice}(HOCH_2CHO)$.

G.2. Matching the $HOCH_2CHO$ Laboratory Spectra to Observations

The spectrum of $HOCH_2CHO$ ice mixed with CO_2 shows a good match to the isolated ice band at 5.72 μm detected with a signal-to-noise ratio of ∼7. Based on the available laboratory spectra for other species, we did not find any other convincing matches to this band (see the upper panel in Figure G3).

We matched the experimental $HOCH_2CHO$:CO_2 spectrum to the intensity of the 5.72 μm ice band and investigated other $HOCH_2CHO$ ice features. The results are illustrated in the lower panel of Figure G3 and discussed in Section 4.5.

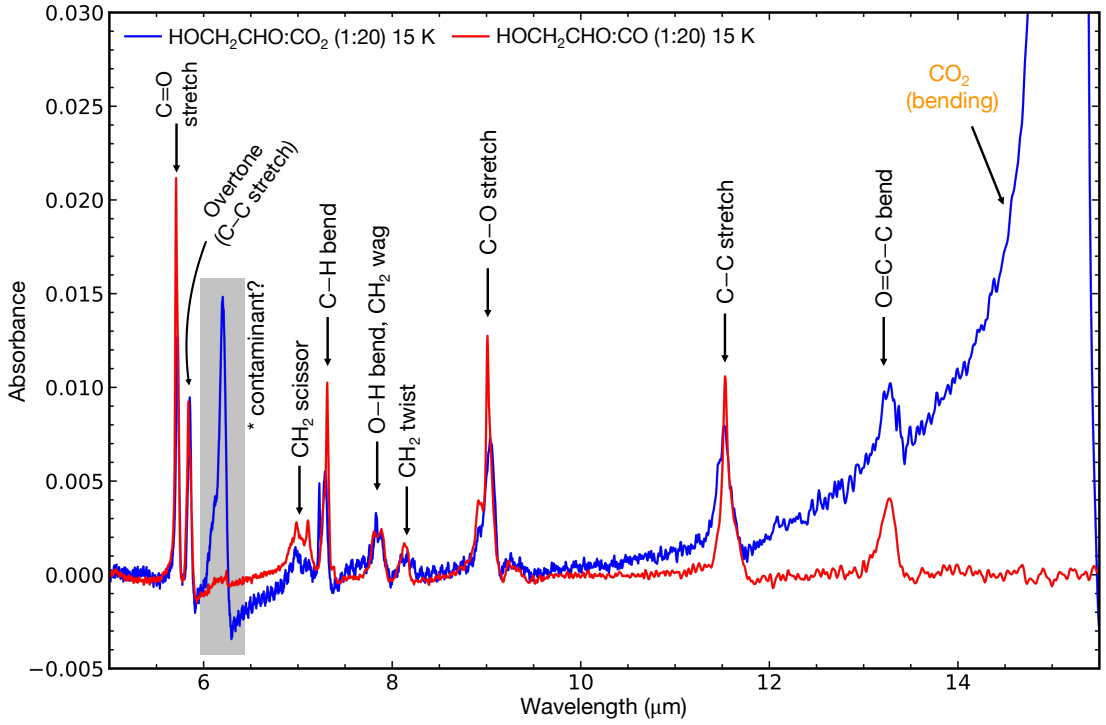


Figure G1. Infrared spectra of $HOCH_2CHO$:CO (1:20) and $HOCH_2CHO$:CO_2 (1:20) at 15 K. The $HOCH_2CHO$ features are indicated with arrows and labeled with their vibrational modes following K. Leroux et al. (2021).

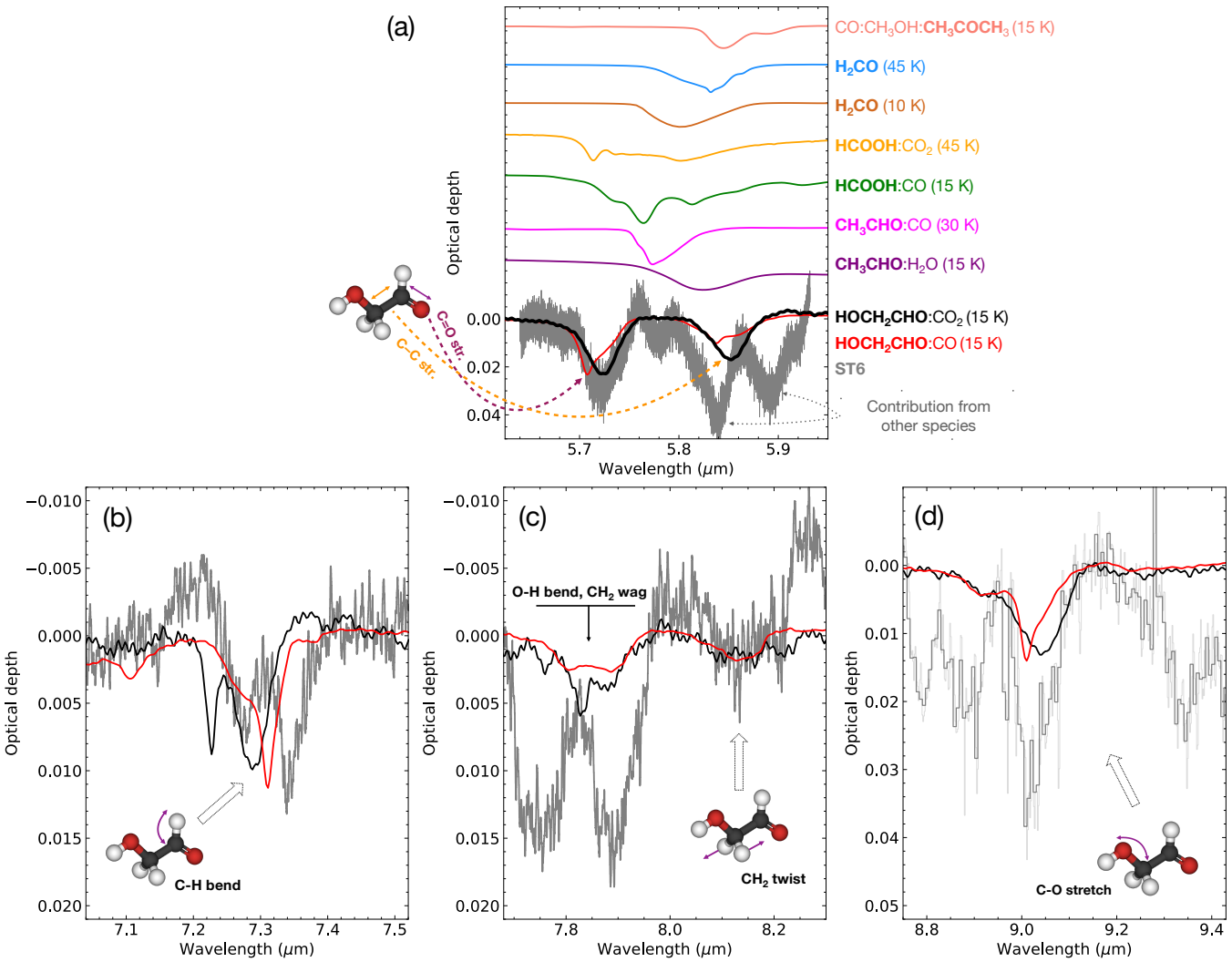


Figure G3. Experimental spectra of glycolaldehyde mixed with CO_2 (black) and CO (red; see Table 2) ices compared (not fitted) to the spectrum of ST6 (gray). The ice features in the laboratory spectra are identified with their vibrational modes following K. Leroux et al. (2021). Panel (a) shows the 5.6–6.0 μm wavelength range covering two $HOCH_2CHO$ ice features (5.72 and 5.86 μm) and displays the laboratory spectra of other COMs for comparison. The laboratory spectra are taken from M. G. Rachid et al. (2020; $CO:CH_3OH:CH_3COCH_3$), J. Terwisscha van Scheltinga et al. (2021; H_2CO), S. E. Bisschop et al. (2007; HCOOH:CO, $HCOOH:CO_2$), and J. Terwisscha van Scheltinga et al. (2018; $CH_3CHO:H_2O$, CH_3CHO:CO). Panels (b)–(d) show other spectral ranges covering additional $HOCH_2CHO$ ice features. Both experimental spectra are scaled to the observed optical depth of the $HOCH_2CHO$ 5.72 μm ice band. The best-fit ENIIGMA model was subtracted from the ST6 spectrum shown in panels (b) and (c); the spectrum was smoothed to highlight the absorption features. In panel (d), the NH_3 ice feature (see Figure E1) was subtracted from the spectrum (light gray) that was subsequently binned by a factor of 4 (dark gray).

G.3. Ice Column Density Determination Based on the 5.72 μm Band

Assuming that $HOCH_2CHO$ is responsible for the 5.72 μm ice band and there is no contribution from other species, we determine the $HOCH_2CHO$ ice column density using the local continuum method. In Figure G2, we illustrate the local continuum subtraction procedure for the 5.62–5.92 μm wavelength range. The continuum-subtracted spectrum is shown in the upper panel of Figure G3.

We obtain the $HOCH_2CHO$ of $(0.09 \pm 0.04) \times 10^{17}$ cm^{-2} by integrating the 5.72 μm band and adopting the band strength of 2.6×10^{-17} cm molecule^{-1} (R. L. Hudson et al. 2005).

Appendix H
Previous Reports on the COM Ice Identification in the JWST MIRI MRS Observations of LMC YSOs

O. Nayak et al. (2024) present a qualitative discussion of the MIRI MRS spectra of 11 YSOs in the star-forming region complex in the southwestern part of the LMC, including K. G. Henize's (1956) optical regions N77, N79, N81, and N83. The spectrum of only one source (YSO Y3) is dominated by prominent ice bands: CH_4 (7.67 μm), NH_3 (9.0 μm), CH_3OH (9.74 μm), and CO_2 (15.27 μm); no column densities are provided.

The YSO Y3 is the youngest of 11 sources discussed by O. Nayak et al. (2024). In addition to these major ice species, O. Nayak et al. (2024) identified an absorption feature at $\sim$13.05 μm in the spectrum of Y3 as the $HCOOCH_3$ absorption band (13.02 μm; J. Terwisscha van Scheltinga et al. 2021); however, at the same time, the authors note that this feature may be an unidentified line. We investigated the spectrum of Y3 based on both the data we reprocessed with a more recent version of the JWST pipeline and the data cubes available in the archive and concluded that the $\sim$13.05 μm absorption line is too narrow to be an ice band. The measured FWHM of 0.00311 μm (O. Nayak et al. 2024; less than two channels in MIRI MRS channel 3) is significantly smaller than

the minimum FWHM of the $HCOOCH_3$ OCO deformation stretching mode at 13.02 μm (0.0262 μm or ∼11 channels) measured in the laboratory by J. Terwisscha van Scheltinga et al. (2021) for pure $HCOOCH_3$ and different $HCOOCH_3$ mixtures at a range of temperatures (15–120 K). The intensity of the narrow ∼13.05 μm feature in the spectrum of Y3 is lower in the reprocessed data and comparable to the intensity of several similarly narrow features in the 12.84–13.08 μm wavelength range.

In the spectrum of the YSO Y1, a more evolved YSO from their sample, O. Nayak et al. (2024) assigned the CH_3CH_2OH ice band identification to a narrow feature at ∼7.23 μm. Based on their laboratory experiments, J. Terwisscha van Scheltinga et al. (2018) provide CH_3CH_2OH band positions and band widths in the mid-infrared for different ice mixtures and temperatures. The minimum FWHM of the CH_3 s–deformation mode at 7.240 μm for pure CH_3CH_2OH or any studied mixture in the 15–160 K temperature range is 0.0171 μm (or 21.4 channels in MIRI MRS channel 1). The FWHM of the ∼7.23 μm absorption feature detected toward Y1 is 0.00661 μm, or 8.3 channels (O. Nayak et al. 2024), indicating that this line is unlikely to be an ice band. The origin of this high signal-to-noise absorption line is unclear.

The absorption feature at 6.12 μm in the spectrum of the same source was identified as the deformation bending mode of solid NH_3 at 6.135 μm (M. Bouilloud et al. 2015); however, this very narrow and faint feature is even less likely to be an ice band. No other ice bands have been detected in the MIRI MRS spectrum of Y1, but it is associated with prominent PAH emission features that make the ice band detection difficult.

ORCID iDs

Marta Sewiło https://orcid.org/0000-0003-2248-6032
Will R. M. Rocha https://orcid.org/0000-0001-6144-4113
Martijn van Gelder https://orcid.org/0000-0002-6312-8525
Maria Gabriela Navarro https://orcid.org/0000-0002-1860-2304
Steven B. Charnley https://orcid.org/0000-0001-6752-5109
Miwha Jin https://orcid.org/0000-0002-4801-436X
Joana M. Oliveira https://orcid.org/0000-0002-0861-7094
Jacco Th. van Loon https://orcid.org/0000-0002-1272-3017
Logan Francis https://orcid.org/0000-0001-8822-6327
Jennifer Wiseman https://orcid.org/0000-0002-1143-6710
Remy Indebetouw https://orcid.org/0000-0002-4663-6827
C.-H. Rosie Chen https://orcid.org/0000-0002-3925-9365
Roya Hamedani Golshan https://orcid.org/0000-0003-1993-2302
Danna Qasim https://orcid.org/0000-0002-3276-4780

References

Abdo, A. A., Ackermann, M., Ajello, M., et al. 2010, A&A, 512, A7
Acharyya, K., & Herbst, E. 2015, ApJ, 812, 142
Argyriou, I., Glasse, A., Law, D. R., et al. 2023, A&A, 675, A111
Argyriou, I., Wells, M., Glasse, A., et al. 2020, A&A, 641, A150
Avni, Y., & Bahcall, J. N. 1980, ApJ, 235, 694
Bennett, C. J., & Kaiser, R. I. 2007, ApJ, 660, 1289
Beuther, H., van Dishoeck, E. F., Tychoniec, L., et al. 2023, A&A, 673, A121
Beuther, H., Zhang, Q., Hunter, T. R., et al. 2004, ApJL, 616, L19
Beuther, H., Zhang, Q., Sridharan, T. K., & Chen, Y. 2005, ApJ, 628, 800
Bisschop, S. E., Fuchs, G. W., Boogert, A. C. A., van Dishoeck, E. F., & Linnartz, H. 2007, A&A, 470, 749
Böker, T., Arribas, S., Lützgendorf, N., et al. 2022, A&A, 661, A82
Boogert, A. C. A., Chiar, J. E., Knez, C., et al. 2013, ApJ, 777, 73
Boogert, A. C. A., Gerakines, P. A., & Whittet, D. C. B. 2015, ARA&A, 53, 541
Boogert, A. C. A., Pontoppidan, K. M., Knez, C., et al. 2008, ApJ, 678, 985
Boogert, A. C. A., Schutte, W. A., Helmich, F. P., Tielens, A. G. G. M., & Wooden, D. H. 1997, A&A, 317, 929
Bottinelli, S., Boogert, A. C. A., Bouwman, J., et al. 2010, ApJ, 718, 1100
Boudin, N., Schutte, W. A., & Greenberg, J. M. 1998, A&A, 331, 749
Bouilloud, M., Fray, N., Bénilan, Y., et al. 2015, MNRAS, 451, 2145
Broadmeadow, A., Sewilo, M., Mundy, L., et al. 2025, ApJ, 991, 59
Browning, M. K., Tumlinson, J., & Shull, J. M. 2003, ApJ, 582, 810
Brunken, N. G. C., van Dishoeck, E. F., Slavicinska, K., et al. 2024, A&A, 692, A163
Bushouse, H., Eisenhamer, J., Dencheva, N., et al. 2024, JWST Calibration Pipeline, v1.13.4, Zenodo, doi:10.5281/zenodo.10569856
Carlson, L. R., Sewiło, M., Meixner, M., Romita, K. A., & Lawton, B. 2012, A&A, 542, A66
Cesaroni, R., Beuther, H., Ahmadi, A., et al. 2019, A&A, 627, A68
Charnley, S. B. 1997, ApJ, 481, 396
Chen, Y., Rocha, W. R. M., van Dishoeck, E. F., et al. 2024, A&A, 690, A205
Christiaens, V., Gonzalez, C., Farkas, R., et al. 2023, JOSS, 8, 4774
Closs, M. F., Ferruit, P., Lobb, D. R., et al. 2008, Proc. SPIE, 7010, 701011
Coutens, A., Persson, M. V., Jørgensen, J. K., Wampfler, S. F., & Lykke, J. M. 2015, A&A, 576, A5
Cuppen, H. M., Linnartz, H., & Ioppolo, S. 2024, ARA&A, 62, 243
Dartois, E., & d'Hendecourt, L. 2001, A&A, 365, 144
Dominik, C., Min, M., & Tazaki, R. 2021, OpTool: Command-line driven tool for creating complex dust opacities, Astrophysics Source Code Library, ascl:2104.010
Dorschner, J., Begemann, B., Henning, T., Jaeger, C., & Mutschke, H. 1995, A&A, 300, 503
Fogerty, S., Forrest, W., Watson, D. M., Sargent, B. A., & Koch, I. 2016, ApJ, 830, 71
Gálvez, O., Maté, B., Herrero, V. J., & Escribano, R. 2010, ApJ, 724, 539
Gardner, J. P., Mather, J. C., Abbott, R., et al. 2023, PASP, 135, 068001
Garrod, R. T., Jin, M., Matis, K. A., et al. 2022, ApJS, 259, 1
Gerakines, P. A., & Hudson, R. L. 2015, ApJL, 808, L40
Gibb, E. L., & Whittet, D. C. B. 2002, ApJL, 566, L113
Gieser, C., Beuther, H., Semenov, D., et al. 2021, A&A, 648, A66
Greenfield, P., & Miller, T. 2016, A&C, 16, 41
Grishunin, K., Weiss, A., Colombo, D., et al. 2024, A&A, 682, A137
Gruendl, R. A., & Chu, Y. 2009, ApJS, 184, 172
Hamedani Golshan, R., Sánchez-Monge, Á., Schilke, P., et al. 2024, A&A, 688, A3
Henize, K. G. 1956, ApJS, 2, 315
Herbst, E., & van Dishoeck, E. F. 2009, ARA&A, 47, 427
Hollis, J. M., Lovas, F. J., & Jewell, P. R. 2000, ApJL, 540, L107
Hudgins, D. M., Sandford, S. A., Allamandola, L. J., & Tielens, A. G. G. M. 1993, ApJS, 86, 713
Hudson, R. L., & Ferrante, R. F. 2020, MNRAS, 492, 283
Hudson, R. L., & Gerakines, P. A. 2019, MNRAS, 485, 861
Hudson, R. L., Gerakines, P. A., & Yarnall, Y. Y. 2024, ApJ, 970, 108
Hudson, R. L., Moore, M. H., & Cook, A. M. 2005, AdSpR, 36, 184
Jäger, C., Dorschner, J., Mutschke, H., Posch, T., & Henning, T. 2003, A&A, 408, 193
Jiménez-Serra, I., Megías, A., Salaris, J., et al. 2025, A&A, 695, A247
Jones, O. C., Woods, P. M., Kemper, F., et al. 2017, MNRAS, 470, 3250
Jørgensen, J. K., Belloche, A., & Garrod, R. T. 2020, ARA&A, 58, 727
Jørgensen, J. K., Harvey, P. M., Evans, N. J., II, et al. 2006, ApJ, 645, 1246
Kemper, F., Vriend, W. J., & Tielens, A. G. G. M. 2004, ApJ, 609, 826
Labiano, A., Argyriou, I., Álvarez-Márquez, J., et al. 2021, A&A, 656, A57
Law, D. R., E. Morrison, J., Argyriou, I., et al. 2023, AJ, 166, 45
Leroux, K., Guillemin, J.-C., & Krim, L. 2021, MNRAS, 507, 2632
Lucke, P. B., & Hodge, P. W. 1970, AJ, 75, 171
Madau, P., & Dickinson, M. 2014, ARA&A, 52, 415
Martín-Doménech, R., Escribano, B., Navarro-Almaida, D., et al. 2025, MNRAS, 541, 2992
McClure, M. K., Rocha, W. R. M., Pontoppidan, K. M., et al. 2023, NatAs, 7, 431
McGuire, B. A. 2022, ApJS, 259, 30
Mehlert, D., Noll, S., Appenzeller, I., et al. 2002, A&A, 393, 809
Meinert, C., Myrgorodska, I., de Marcellus, P., et al. 2016, Sci, 352, 208
Meixner, M., Gordon, K. D., Indebetouw, R., et al. 2006, AJ, 132, 2268
Meixner, M., Panuzzo, P., Roman-Duval, J., et al. 2013, AJ, 146, 62
Mie, G. 1908, AnP, 330, 377
Nayak, O., Hirschauer, A. S., Kavanagh, P. J., et al. 2024, ApJ, 963, 94

Nguyen, T., Oba, Y., Sameera, W. M. C., Furuya, K., & Watanabe, N. 2024, ApJ, 976, 250
Novozamsky, J. H., Schutte, W. A., & Keane, J. V. 2001, A&A, 379, 588
Öberg, K. I. 2016, ChRv, 116, 9631
Öberg, K. I., & Bergin, E. A. 2021, PhR, 893, 1
Oliveira, J. M., van Loon, J. T., Chen, C.-H. R., et al. 2009, ApJ, 707, 1269
Oliveira, J. M., van Loon, J. T., Sewiło, M., et al. 2019, MNRAS, 490, 3909
Oliveira, J. M., van Loon, J. T., Sloan, G. C., et al. 2011, MNRAS, 411, L36
Oliveira, J. M., van Loon, J. T., Stanimirović, S., & Zijlstra, A. A. 2006, MNRAS, 372, 1509
Ott, J., Henkel, C., Staveley-Smith, L., & Weiß, A. 2010, ApJ, 710, 105
Pei, Y. C., Fall, S. M., & Hauser, M. G. 1999, ApJ, 522, 604
Pietrzyński, G., Graczyk, D., Gallenne, A., et al. 2019, Natur, 567, 200
Potapov, A., Linz, H., Bouwman, J., et al. 2025, A&A, 697, A53
Qin, S.-L., Liu, T., Liu, X., et al. 2022, MNRAS, 511, 3463
Rachid, M. G., Terwisscha van Scheltinga, J., Koletzki, D., & Linnartz, H. 2020, A&A, 639, A4
Rigby, J., Perrin, M., McElwain, M., et al. 2023, PASP, 135, 048001
Robitaille, T., & Bressert, E. 2012, APLpy: Astronomical Plotting Library in Python, Astrophysics Source Code Library, ascl:1208.017
Rocha, W. R. M., McClure, M. K., Sturm, J. A., et al. 2025, A&A, 693, A288
Rocha, W. R. M., Perotti, G., Kristensen, L. E., & Jørgensen, J. K. 2021, A&A, 654, A158
Rocha, W. R. M., Pilling, S., de Barros, A. L. F., et al. 2017, MNRAS, 464, 754
Rocha, W. R. M., Rachid, M. G., McClure, M. K., He, J., & Linnartz, H. 2024a, A&A, 681, A9
Rocha, W. R. M., van Dishoeck, E. F., Ressler, M. E., et al. 2024b, A&A, 683, A124
Roman-Duval, J., Gordon, K. D., Meixner, M., et al. 2014, ApJ, 797, 86
Russell, S. C., & Dopita, M. A. 1992, ApJ, 384, 508
Sasaki, M., Breitschwerdt, D., Baumgartner, V., & Haberl, F. 2011, A&A, 528, A136
Schutte, W. A., Boogert, A. C. A., Tielens, A. G. G. M., et al. 1999, A&A, 343, 966
Seale, J. P., Looney, L. W., Chen, C. H. R., Chu, Y.-H., & Gruendl, R. A. 2011, ApJ, 727, 36
Seale, J. P., Looney, L. W., Chu, Y.-H., et al. 2009, ApJ, 699, 150
Seale, J. P., Meixner, M., Sewiło, M., et al. 2014, AJ, 148, 124
Sewiło, M., Charnley, S. B., Schilke, P., et al. 2019, ESC, 3, 2088
Sewiło, M., Cordiner, M., Charnley, S. B., et al. 2022, ApJ, 931, 102
Sewiło, M., Indebetouw, R., Charnley, S. B., et al. 2018, ApJL, 853, L19
Shimonishi, T., Dartois, E., Onaka, T., & Boulanger, F. 2016a, A&A, 585, A107
Shimonishi, T., Das, A., Sakai, N., et al. 2020, ApJ, 891, 164
Shimonishi, T., Izumi, N., Furuya, K., & Yasui, C. 2021, ApJ, 922, 206
Shimonishi, T., Onaka, T., Kato, D., et al. 2008, ApJL, 686, L99
Shimonishi, T., Onaka, T., Kato, D., et al. 2010, A&A, 514, A12
Shimonishi, T., Onaka, T., Kawamura, A., & Aikawa, Y. 2016b, ApJ, 827, 72
Shingledecker, C. N., Lamberts, T., Laas, J. C., et al. 2020, ApJ, 888, 52
Slavicinska, K., Boogert, A. C. A., Tychoniec, Ł., et al. 2025a, A&A, 693, A146
Slavicinska, K., Tychoniec, Ł., Navarro, M. G., et al. 2025b, ApJL, 986, L19
Smith, R. C. & MCELS Team 1998, PASA, 15, 163
Taquet, V., López-Sepulcre, A., Ceccarelli, C., et al. 2015, ApJ, 804, 81
Terwisscha van Scheltinga, J., Ligterink, N. F. W., Boogert, A. C. A., van Dishoeck, E. F., & Linnartz, H. 2018, A&A, 611, A35
Terwisscha van Scheltinga, J., Marcandalli, G., McClure, M. K., Hogerheijde, M. R., & Linnartz, H. 2021, A&A, 651, A95
Toribio San Cipriano, L., Domínguez-Guzmán, G., Esteban, C., et al. 2017, MNRAS, 467, 3759
van Broekhuizen, F. A., Pontoppidan, K. M., Fraser, H. J., & van Dishoeck, E. F. 2005, A&A, 441, 249
van Dishoeck, E. F., Tychoniec, Ł., Rocha, W. R. M., et al. 2025, A&A, 699, A361
van Gelder, M. L., Tabone, B., Tychoniec, Ł., et al. 2020, A&A, 639, A87
van Gelder, M. L., Tabone, B., van Dishoeck, E. F., & Godard, B. 2021, A&A, 653, A159
van Loon, J. T., Oliveira, J. M., Gordon, K. D., Sloan, G. C., & Engelbracht, C. W. 2010a, AJ, 139, 1553
van Loon, J. T., Oliveira, J. M., Gordon, K. D., et al. 2010b, AJ, 139, 68
van Loon, J. T., Oliveira, J. M., Wood, P. R., et al. 2005, MNRAS, 364, L71
Wells, M., Pel, J. W., Glasse, A., et al. 2015, PASP, 127, 646
Welty, D. E., Federman, S. R., Gredel, R., Thorburn, J. A., & Lambert, D. L. 2006, ApJS, 165, 138
Whitney, B. A., Sewilo, M., Indebetouw, R., et al. 2008, AJ, 136, 18
Wong, T., Hughes, A., Ott, J., et al. 2011, ApJS, 197, 16
Wright, G. S., Rieke, G. H., Glasse, A., et al. 2023, PASP, 135, 048003